

The Pennsylvania State University
The Graduate School
College of Earth and Mineral Sciences

**MECHANISMS OF SINTERING AND SECOND PHASE
FORMATION IN BAYER ALUMINA**

A Dissertation in
Materials Science and Engineering
by
Tobias Frueh

© 2017 Tobias Frueh

Submitted in Partial Fulfillment
of the Requirements
for the Degree of

Doctor of Philosophy

September 2017

The dissertation of Tobias Frueh was reviewed and approved* by the following:

Gary Messing

Distinguished Professor of Ceramic Science and Engineering

Thesis Advisor, Chair of Committee

James Adair

Professor of Materials Science and Engineering, Biomedical Engineering and
Pharmacology

Optional Title Here

John Hellmann

Professor of Materials Science and Engineering

Associate Dean for Graduate Education and Research

Douglas Wolfe

Associate Professor of Materials Science and Engineering

Department Head, Advanced Coatings at the Applied Research Laboratory

Senior Scientist

*Signatures are on file in the Graduate School.

Abstract

Table of Contents

List of Figures	vi
List of Tables	viii
Acknowledgments	ix
Chapter 1	
Introduction	2
1.1 section1.1	2
1.1.1 subsection1.1.1	2
Chapter 2	
The Effects of Na₂O and SiO₂ on Liquid Phase Sintering of Bayer Al₂O₃	3
2.1 Introduction	3
2.2 Experimental	4
2.3 Results	5
2.3.1 Effects of Na ₂ O-doping	5
2.3.2 Effects of Na ₂ O/SiO ₂ co-doping	6
2.4 Discussion	7
2.5 Summary	12
Chapter 3	
Powder Chemistry Effects on the Sintering Behavior of MgO-doped Bayer Alumina	25
3.1 Introduction	25
3.2 Experimental	27
3.3 Computational Methodology	28
3.4 Sintering and Microstructure Analysis	30
3.5 Mechanistic Interpretation	33

3.6 Summary and Conclusion	38
Chapter 4	
Powder Chemistry Effects on Grain Boundaries During Densification of Bayer Alumina	55
4.1 Introduction	55
4.2 More Declaration	55
Chapter 5	
β-Al₂O₃: A Model System for the Formation of Second Phases in Al₂O₃	57
5.1 Introduction	57
5.2 More Declaration	57
Chapter 6	
IChallenges and Opportunities of Master Sintering Curve Analysis of Sintering Processes	59
6.1 Introduction	59
6.2 Experimental	59
Chapter 7	
Summary and Future Work	60
7.1 Introduction	60
7.2 More Declaration	60
Bibliography	62

List of Figures

2.1	SEM image of as-received chemically purified Bayer Al ₂ O ₃ powder used in this study.	16
2.2	Dilatometer curves of as-received and singly Na ₂ O-doped samples heated at 10°C/min to 1525°C.	17
2.3	Densification kinetics of Bayer Al ₂ O ₃ doped with different Na ₂ O concentrations and sintered at 1525°C.	18
2.4	Microstructures of as-received and singly 529 ppm Na ₂ O doped samples after 30 min, 3 h and 8 h at 1525°C.	19
2.5	Dilatometer curves of as-received, singly SiO ₂ -doped, and Na ₂ O/SiO ₂ -doped Bayer Al ₂ O ₃ heated at 10°C/min to 1525°C.	20
2.6	Densification kinetics of Bayer Al ₂ O ₃ doped with different concentrations of Na ₂ O and SiO ₂ at 1525°C.	21
2.7	Microstructures of Bayer Al ₂ O ₃ doped with a) 603 ppm SiO ₂ and b) 529 ppm Na ₂ O and 603 ppm SiO ₂ after heating at 1525°C for 8h.	22
2.8	Micrographs of a sample doped with 1029 ppm Na ₂ O after sintering at 1525°C for 3Åäh. The micrographs were recorded using a) a secondary electron detector and b) a backscattered electron detector. The arrows point at the platelet shaped beta alumina grains that form in samples doped with Na ₂ O. The samples were not thermally etched.	23
2.9	Liquidus projection of the Al ₂ O ₃ -SiO ₂ -Na ₂ O ternary phase diagram. The red solid lines are isoplethal cuts representing the samples investigated in this study. The red dashed line is the 1525°C isotherm where α -Al ₂ O ₃ and liquid are in equilibrium. The blue dash-dot line and green dotted line are eutectic lines at which α -Al ₂ O ₃ and liquid is in equilibrium with β -Al ₂ O ₃ or mullite, respectively.	24
3.1	SEM image of 380 ppm MgO-doped specialty alumina powder used in this work.	43

3.2 Dilatometer curves of a) 380 ppm MgO-doped and b) MgO-free [1] specialty alumina samples with different Na ₂ O/SiO ₂ levels heated at 10°C/min to 1525°C.	44
3.3 Densification kinetics of specialty processed alumina containing different amounts Na ₂ O and SiO ₂ and a) 380 ppm MgO sintered at 1450°C, b) 380 ppm MgO sintered at 1525°C, and c) 2 ppm MgO sintered at 1525°C [1].	45
3.4 Microstructures of 380 ppm MgO-doped specialty alumina samples with different Na ₂ O and SiO ₂ concentrations sintered at 1525°C for 8 h.	46
3.5 Sintering trajectories (grain size vs. relative density) for 380 ppm MgO-doped specialty alumina samples with different Na ₂ O and SiO ₂ concentrations.	47
3.6 Grain boundary of a sample containing 529 ppm Na ₂ O, 603 ppm SiO ₂ , and 2 ppm MgO after 3 h at 1525°C.	48
3.7 Grain boundaries of samples containing 560 ppm Na ₂ O, 582 ppm SiO ₂ , and 380 ppm MgO after a) 0 h and b) 3 h at 1525°C.	49
3.8 EDS of grain boundaries of samples containing 560 ppm Na ₂ O, 582 ppm SiO ₂ , and 380 ppm MgO after a) 0 h and b) 3 h at 1525°C showing the Si distribution. After 0 h Si shows a stronger segregation to the grain boundaries than after 3 h.	50
3.9 EDS line scan across a grain boundary of a sample containing 560 ppm Na ₂ O, 582 ppm SiO ₂ , and 380 ppm MgO after sintering at 1525°C for a) 0 h and b) 3 h.	51
3.10 Comparison of the formation energy of alpha-Al ₂ O ₃ with an Mg-cluster (E_{Form}^{Mg}), Si-cluster (E_{Form}^{Si}) and Mg+Si-cluster (E_{Form}^{Mg+Si}) as a function of temperature. The formation energy difference (ΔE_{Form}) between the structures was calculated from Eq. REF to compare the formation energy values and show that it is energetically favorable to form Mg+Si-clusters over Si-clusters and Mg-clusters.	52
3.11 EDS maps of different oxides in 380 ppm MgO-doped specialty alumina samples after sintering at 1525°C for a-d) 0 h and e-h) 3 h.	53
3.12 Na ₂ O concentration (ICP measurements) of 380 ppm MgO-doped specialty alumina samples with 560 ppm Na ₂ O as a) function of sintering temperature and b) as a function of sintering time at 1525 °C.	54

List of Tables

2.1	Physical and chemical characteristics of the as-received Bayer Al ₂ O ₃ powder used in this study.	14
2.2	Calculated compositions and amounts of liquid in as-received, singly doped and co-doped samples at 1525°C ($\alpha = \alpha\text{-Al}_2\text{O}_3$, $\beta = \beta\text{-Al}_2\text{O}_3$, L= liquid, M = mullite).	15
3.1	Physical and chemical characteristics of the as-received 380 ppm MgO-doped specialty alumina powder used in this study.	40
3.2	Calculated compositions and amounts of liquid in 380 ppm MgO-doped specialty alumina samples of different chemistries at 1450°C and 1525 °C.	41
3.3	Lattice parameters and equilibrium energy (E_0) compared to previous first-principles and experimental values.	42

Acknowledgments

Dedication

Chapter 1

Introduction

1.1 section1.1

Pestorius [200] developed an algorithm to investigate propagation of finite-amplitude noise in pipes. His algorithm, based on weak shock theory, includes the effects of nonlinearity and tube wall boundary layer attenuation and dispersion. The hybrid time-frequency domain algorithm applies nonlinearity in the time domain, applies a fast Fourier transform (FFT), and then applies attenuation and dispersion in the frequency domain. Then an inverse FFT is taken to return to the time domain to propagate to the next step.

1.1.1 subsection1.1.1

Chapter 2 |

The Effects of Na₂O and SiO₂

on Liquid Phase Sintering of Bayer

Al₂O₃

2.1 Introduction

Al₂O₃ is arguably the most extensively used and researched ceramic material because it is used in many large volume applications such as high temperature refractories, technical ceramics, high voltage insulators, and functional fillers. The majority of Al₂O₃ applications use synthetic or specialty aluminas derived from Bayer feedstocks, such as aluminum trihydrate (Al(OH)₃), smelter grade Al₂O₃ and others. Bayer process aluminas are typically 99.0 - 99.9% pure and contain Na₂O, CaO, Fe₂O₃, and SiO₂ impurities that originate from the bauxite ore and/or Bayer process reagents (e.g., NaOH). The vast majority of research on the sintering of Al₂O₃, however, focuses on ultra-high purity ($\geq 99.99\%$) aluminas derived from specialty feedstocks, such as ammonium alum (NH₄Al(SO₄)₂·12H₂O), boehmite (γ -AlOOH) and aluminum chloride (AlCl₃). While ultra-high purity aluminas provide the purest platform from which to conduct fundamental sintering research, that research does not usually explore the types and amounts of impurities typical of Bayer aluminas. Commercial Bayer Al₂O₃ powders exist in a range of reactive grades that differ in the amount and types of these impurities. Therefore, the evaluation of specialty reactive aluminas, within the context of previous work on ultra-high purity aluminas, is a valuable contribution to industrial users and bridges

fundamental sintering research with ultra-high purity aluminas.

2.2 Experimental

A chemically purified 0.4 μm median particle size Bayer process Al_2O_3 powder (Almatis, Inc., Leetsdale, PA, USA) with only 2 ppm MgO was used to study the sintering of near MgO -free Bayer Al_2O_3 (Figure 2.1). The powder was chemically purified by the manufacturer so that impurity levels similar to commercial high purity Bayer process aluminas were obtained after doping with Na_2O and/or SiO_2 . The physical and chemical characteristics of the as-received powder are shown in Table 2.1. Chemical analysis of the as-received Al_2O_3 was performed by inductively coupled plasma (ICP) emission spectroscopy (iCap 6000, Thermo Fischer Scientific, Inc., Waltham, MA, USA) after Al_2O_3 samples were acid digested in a microwave digestion unit in a TeflonTM sample holder. It should be noted that the as-received Bayer Al_2O_3 contained impurity levels of 90 ppm Fe_2O_3 , 62 CaO , and 22 ppm TiO_2 . The Na_2O and SiO_2 reported after doping include the impurity concentrations in the as-received powder (29 ppm Na_2O and 103 ppm SiO_2).

The Al_2O_3 powders were doped with up to 1000 ppm Na_2O using sodium acetate ($\text{NaC}_2\text{H}_3\text{O}_2 \cdot 3\text{H}_2\text{O}$, ACS grade, BDH, West Chester, PA, USA), based on the procedure reported by Louet et al. [2]. The Al_2O_3 powders were dispersed in a solution of sodium acetate dissolved in de-ionized water. The suspension was stirred on a magnetic stir plate for 5 h at room temperature, and held at 80°C for 24 h while stirring until the mixture was too viscous to stir, and then dried at 100°C for 24 h.

Samples were doped with up to 500 ppm SiO_2 by first dissolving tetraethyl orthosilicate (TEOS, $\text{Si}(\text{OC}_2\text{H}_5)_4$, 98%, Aldrich Chemical Company, Inc., Milwaukee, WI, USA) in 200 proof ethanol with a few drops of de-ionized water to hydrolyze the TEOS and immediately mixed at room temperature for 5 h with either the as-received or Na_2O -doped Al_2O_3 powder. The mixture was subsequently stirred at 70°C for an additional 12 h. The powder was then dried at 100°C for 2 h, followed by crushing in a mortar and pestle, and sieving to -106 μm (US Standard 140 mesh).

Samples were prepared for sintering studies by uniaxially dry pressing the powders at 170 MPa and then cold isostatic pressing at 200 MPa (CIP, Autoclave

Engineers, Erie, PA, USA) to obtain cylindrical samples (3.0-3.5 mm long by 12.7 mm diameter or 8.5-10 mm long by 6 mm diameter) with green densities of 59.0% \pm 0.5% of theoretical density. To investigate the sintering process, dry pressed 8.5-10 mm long by 6 mm diameter cylinders were heated at 10°C/min to 1525°C in a thermomechanical analyzer (TMA, Linseis PT1600, Robbinsville, NJ, USA). The kinetics of sintering and grain growth were evaluated on 3.0-3.5 mm long by 12.7 mm diameter samples heated at 10°C/min to 1200 °C then 5°C/min to 1525°C followed by sintering at 1525°C for up to 8 h. The density of three samples of each condition was measured by the Archimedes method according to ASTM standard B962-15 [3] and the average density reported for each sintering time and temperature. For microstructure analysis, samples were first polished to a surface finish of 1 μ m and then thermally etched in air at 1425°C for 40 min. Average grain sizes were measured on SEM (ESEM, Quanta 200, FEI Company, Hillsboro, OR, USA) micrographs using a linear intercept method (ASTM Standard E112-96) [4].

2.3 Results

2.3.1 Effects of Na₂O-doping

The doping experiments were designed to uniformly distribute Na₂O and SiO₂ on the surfaces of the Al₂O₃ particles. Upon heating the dopant NaC₂H₃O₂·3H₂O first dehydrates and then decomposes to form Na₂CO₃ above 385°C [5]. Using a video recorder, we observed that anhydrous sodium acetate melts and rapidly spreads on the surface of an Al₂O₃ substrate at \sim 420°C. Na₂CO₃ melts at 851°C and subsequently decomposes to Na₂O [5]. As a result of the rapid wetting of the Na₂O precursor on the Al₂O₃ substrate we conclude that Na₂O is uniformly distributed on the powder surface by the acetate doping process.

Figure 2.2 shows the shrinkage behavior of Bayer Al₂O₃ doped with different Na₂O concentrations during heating to 1525°C at 10°C/min. The as-received Al₂O₃ (intrinsic impurities: 29 ppm Na₂O, 103 ppm SiO₂) begins to shrink at \sim 1050 °C, whereas shrinkage begins at 1100°C for samples doped with 1029 ppm Na₂O. The difference in density at the beginning of densification continues throughout the heating cycle. However, above \sim 1350°C the densification rate of the Na₂O doped samples surpasses that of the as-received sample. Overall, the Na₂O-doped samples

are 2.5% less dense than the as-received Al_2O_3 after heating to 1525°C.

Figure 2.3 shows the influence of Na_2O concentration on the densification kinetics at 1525°C. Clearly, the degree of densification decreases with increasing Na_2O concentration for up to 30 min with the Na_2O -doped samples being as much as 2% less dense than the as-received Al_2O_3 . However, after ≥ 30 min at 1525°C densification is independent of Na_2O content and all samples are 97.5-98.0% dense after ≥ 3 h.

The microstructures of as-received samples (29 ppm Na_2O) and samples doped with 529 ppm Na_2O sintered for 30 min, 3 h and 8 h at 1525°C are compared in Figure 2.4. It is seen that higher Na_2O concentration does not affect the average grain size for all hold times. Microstructures of as-received samples are predominantly equiaxed with a small number of faceted grains, whereas samples doped with Na_2O appear to have an increasing number of faceted grain boundaries with increasing Na_2O concentration. A few tabular grains of up to $60 \mu\text{m}$ were seen in both as-received and Na_2O -doped samples after 8 h at 1525°C (see Figure 2.4c and 2.4f). Those faceted grains are larger in the as-received powder samples compared to Na_2O -doped samples, whereas the Na_2O -doped samples show more large tabular grains than samples from the as-received powder.

2.3.2 Effects of $\text{Na}_2\text{O}/\text{SiO}_2$ co-doping

As seen in Figure 2.5, the presence of 603 ppm SiO_2 significantly retards densification of as-received alumina. Starting at $\sim 1250^\circ\text{C}$, all of the SiO_2 -doped samples densify less than as-received and singly Na_2O -doped samples. The densification rate of the SiO_2 -doped samples from 1250 to 1525°C is slower than the as-received alumina. SiO_2 reduces the linear shrinkage by $\sim 3.0\%$ and thus the samples are 8.7% less dense than the as-received Al_2O_3 after 8 h at 1525°C.

The densification kinetics of the Al_2O_3 powders doped with different amounts of Na_2O (154 and 529 ppm) and SiO_2 (203 and 603 ppm) are compared in Figure 2.6. It is seen that the addition of SiO_2 significantly reduces sintered density for all hold times. For example, samples containing as much as 603 ppm SiO_2 have densities of 81.5% after 0 h and 93.8% after 8 h at 1525°C, whereas the as-received and singly Na_2O -doped Al_2O_3 samples are 98% dense after 3 h at 1525°C.

Figure 2.6 shows the effect of Na_2O on the densification of SiO_2 -doped samples.

For hold times < 1 h, samples doped with 529 ppm Na₂O and 203 ppm SiO₂ are ~ 1.5% denser than samples doped with 154 ppm Na₂O and 203 ppm SiO₂. A difference in Na₂O concentration does not affect the final density of samples containing 203 ppm SiO₂ (96.5 - 97.0%) after 3 h at 1525°C. For higher SiO₂ concentrations (603 ppm), singly SiO₂ doped samples are 1 - 2.5% less dense than samples co-doped with 529 ppm Na₂O and 603 ppm SiO₂ for all hold times at 1525°C.

The average grain sizes of the as-received and Na₂O-doped samples are nominally the same and increase from 1.6 μm to 2.5 μm after 30 min and 8 h at 1525°C, respectively. There was little grain growth (1.4 μm to 2.1 μm) in singly SiO₂-doped samples (603 ppm) after 30 min and 8 h at 1525°C, respectively. In samples co-doped with 529 ppm Na₂O and 603 ppm SiO₂ the average grain size is 1.6 μm for hold times between 30 min and 8 h at 1525°C. The limited grain growth is attributed primarily to the large fraction of porosity. Micrographs of 603 ppm SiO₂ singly doped and 529 ppm Na₂O and 603 ppm SiO₂ co-doped samples heated for 8 h after heating for 8 h at 1525°C are compared in Figure 2.7. Both samples are only 92-94% dense and thus it was difficult to prepare polished micrographs without some grain pull-out.

2.4 Discussion

To understand the above effects, we first note from the Al₂O₃-Na₂O phase diagram [6] that Na₂O is insoluble in α -Al₂O₃. A few platelet shaped grains with high aspect ratios were observed in the microstructures of sintered Na₂O-doped samples (Figure 2.8). Due to their morphology and literature reports, [7-11] it is assumed that these grains are a type of β -Al₂O₃. Four types of β -Al₂O₃ exist; two of them, β -Al₂O₃ (Na₂O·11Al₂O₃) and β'' -Al₂O₃ (Na₂O·5Al₂O₃), form in the binary system Na₂O-Al₂O₃ [12, 13]. The determination of which type of β -Al₂O₃ forms and the conditions of formation were not the subject of this work, so these analyses were not performed.

Sodium aluminate (NaAlO₂) is reported to form at temperatures as low as 900°C, [14] and β'' -Al₂O₃ (Na₂O·5Al₂O₃) can be synthesized at temperatures as low as 1100 °C [7, 15, 16]. Therefore, we hypothesize that either sodium aluminate or β'' -Al₂O₃ forms before the onset of densification and that the presence of the

second phases on the surface of the Al₂O₃ particles retards the initial shrinkage of Na₂O-doped samples at \sim 1050°C. However, we did not observe any β -Al₂O₃ type grains in the samples at this temperature. Alternatively, as discussed below, Na₂O may interact with the 103 ppm of intrinsic SiO₂ in the sample.

We hypothesize that the initial grain boundaries in the as-received Al₂O₃ are wetted with the intrinsic impurities such as Na₂O, CaO, TiO₂ and SiO₂. Doping with Na₂O and SiO₂ changes the relative grain boundary chemistries and the properties of the respective grain boundary liquids. In the presence of a grain boundary liquid, densification occurs by a solution-precipitation sintering process, and thus, the rate of densification is controlled by either interface reaction between the grain boundary liquid and Al₂O₃ grains, or by the diffusion of Al³⁺ through the liquid grain boundary film. Al³⁺ diffusion is rate-limiting at 1525°C since it has been shown for molten glass systems that Al³⁺ has lower ionic diffusion rates than O²⁻ [17]. For diffusion-controlled densification, the densification rate is given by [18, 19]

$$\frac{d\left(\frac{\Delta\rho}{\rho}\right)}{dt} = \frac{A\delta D_l C_0 \gamma_{lv} \Omega}{kT} r_s^{-4} \quad (2.1)$$

and for interface reaction-controlled densification, the densification rate is given by

$$\frac{d\left(\frac{\Delta\rho}{\rho}\right)}{dt} = \frac{B K C_0 \gamma_{lv} \Omega}{kT} r_s^{-2} \quad (2.2)$$

where A and B are geometric factors, δ is the thickness of the liquid film, D_l is the diffusion coefficient of Al³⁺ in the liquid, C_o is the equilibrium solute concentration, K the interface reaction constant, γ_{lv} is the liquid surface tension, Ω is the molecular volume of the solid, r_s is the particle radius, k is the Boltzmann constant and T is absolute temperature.

Equations 2.1 and 2.2 can be used to gain insights into the rate-limiting densification mechanisms during liquid phase sintering by evaluating their ratio [18, 19]

$$\alpha = \frac{A\delta D_l}{B K} r_s^{-2} \quad (2.3)$$

In general, for $\alpha > 1$, densification is controlled by the interface reaction, since D_l is relatively high. For $\alpha < 1$, densification is controlled by diffusion, and for $\alpha = 1$ both mechanisms contribute equally to densification [19]. Since the product

of the grain boundary thickness and the diffusion coefficient greatly influences the rate-determining mechanism, δD_l and the interface reaction constant K were examined in more detail.

Because the main impurities in Bayer aluminas are SiO_2 and Na_2O , the Al_2O_3 - SiO_2 - Na_2O ternary phase diagram [6] was utilized to evaluate the effects of dopant type and concentration on solubility of Al_2O_3 in the grain boundary liquid. It is assumed that the system approaches thermodynamic equilibrium upon holding at 1525°C, and thus the equilibrium composition of the liquid at 1525°C can be calculated from the ternary phase diagram (Figure 2.9). For simplification, we considered only Al_2O_3 , SiO_2 and Na_2O for the analysis, and assumed that all impurities/dopants are located in the grain boundaries. It was stated earlier that Na_2O is not soluble in Al_2O_3 , and it has been reported in the literature that SiO_2 segregates at the grain boundaries in Al_2O_3 [20]. Figure 2.9 shows the liquidus projection of the Al_2O_3 - SiO_2 - Na_2O ternary phase diagram. The red solid lines connecting the Al_2O_3 end member to the Na_2O - SiO_2 side are binary cuts through the ternary (isoplethal sections) and correspond to some of the $\text{Na}_2\text{O}/\text{SiO}_2$ ratios investigated in this study. The red dashed line is the isotherm at 1525°C for the part of the phase diagram where α - Al_2O_3 and liquid are in equilibrium. The blue dash-dot line and the green dotted line are eutectic lines along which β - Al_2O_3 or mullite is stable with α - Al_2O_3 and a liquid. The isotherm and the eutectic lines are important for determining the stable phases and the composition of the liquid in the samples. If a binary cut intersects the isotherm (red dashed line) only α - Al_2O_3 and liquid are stable phases at 1525°C and the intersection point determines the composition of the liquid. If a binary cut intersects one of the two marked eutectic lines (blue dash-dot or green dotted) a third phase (β - Al_2O_3 or mullite) is stable in those samples, and the composition of the liquid at 1525°C is determined by the intersection point of the respective intersected eutectic line with the isotherm at 1525°C.

The Al_2O_3 - SiO_2 - Na_2O phase diagram demonstrates that a small amount of liquid is stable at 1525°C for all compositions investigated. Note that these overall compositions are all very close to the Al_2O_3 end member ($\sim 99.8\%$ Al_2O_3) and Na_2O and SiO_2 are insoluble in Al_2O_3 . Isoplethal sections (red solid lines in Figure 2.9) can be used to determine the stability and equilibrium composition of a liquid since the volume fractions of Na_2O and SiO_2 are known. Lambotte and

Chartrand [6] calculated isoplethal sections of the ternary phase diagram, and based on their calculations, the solubility of Al_2O_3 in the liquid at 1525°C in the samples was estimated based on the respective $\text{Na}_2\text{O}:\text{SiO}_2$ ratios (assuming a constant liquid density of 2.45 g/cm [4, 21]). Likewise, the volume fractions of liquid and solid phases can be estimated since the doping and impurity concentrations of SiO_2 and Na_2O are known. Table 2.2 summarizes the stable phases, the liquid compositions, and the total amount of liquid in the as-received and doped samples. Stable liquids at 1525°C are predicted for liquid compositions with $\text{Na}_2\text{O}:\text{SiO}_2$ ratios between 0.25 and 0.5. As described above, for higher Na_2O concentrations in the samples (global $\text{Na}_2\text{O}:\text{SiO}_2$ ratio > 0.5), $\alpha\text{-Al}_2\text{O}_3$, $\beta\text{-Al}_2\text{O}_3$ and a liquid with a $\text{Na}_2\text{O}:\text{SiO}_2$ ratio of 0.5 are stable. For sample compositions with higher SiO_2 concentrations (global $\text{Na}_2\text{O}:\text{SiO}_2$ ratio < 0.25) $\alpha\text{-Al}_2\text{O}_3$, mullite and a liquid with a $\text{Na}_2\text{O}:\text{SiO}_2$ ratio of 0.25 are stable. Since the global $\text{Na}_2\text{O}:\text{SiO}_2$ ratio in most of the samples investigated in this work is either > 0.5 or < 0.25, the liquid in those samples had compositions of 0.5 or 0.25, respectively. As the $\text{Na}_2\text{O}:\text{SiO}_2$ ratio in the liquid increases from 0.25 to 0.5 the solubility of Al_2O_3 in the liquid increases from 18.4 vol.% to 21.6 vol.% [6]. The increased Al_2O_3 solubility leads to higher densification rates and higher densities in $\text{Na}_2\text{O}/\text{SiO}_2$ co-doped samples compared to singly SiO_2 -doped samples, regardless of the rate-limiting process.

Assuming fully dense samples and the liquid volume fractions reported in Table 2.2, we calculated the grain boundary thickness δ using:

$$\delta = 2 \frac{V_g \phi}{S_g (1 - \phi)} \quad (2.4)$$

where ϕ is the liquid volume fraction and V_g and S_g are the volume and the surface area based on the average grain size, respectively. For as-received and singly Na_2O -doped samples the grain boundary thickness is < 0.3 nm for all observed grain sizes. For $\text{Na}_2\text{O}/\text{SiO}_2$ -co-doped samples (603 ppm SiO_2) the grain boundary thickness is between 0.8 and 1.8 nm for grain sizes of 1 μm and 2.5 μm , respectively. The calculated grain boundary thickness of singly SiO_2 -doped samples is similar to that of as-received samples, since mullite is predicted to form in the $\text{Al}_2\text{O}_3\text{-SiO}_2\text{-Na}_2\text{O}$ system for low Na_2O concentrations at 1525°C. However, mullite may not form in Bayer process Al_2O_3 due to the presence of other impurities, such as CaO , which, similar to Na_2O , lowers the eutectic temperature and acts as a network modifier

in the glass. Therefore, the grain boundary thicknesses of singly SiO_2 -doped and $\text{Na}_2\text{O}/\text{SiO}_2$ co-doped samples are expected to be similar at ~ 1.8 nm. The amount of liquid in the samples and, therefore, the grain boundary thickness, is governed mainly by the amount of glass forming species in the samples, i.e. SiO_2 .

The diffusion coefficient of Al^{3+} through the liquid grain boundary phase can be calculated with the Eyring relation

$$D_l = \frac{kT}{\eta\lambda} \quad (2.5)$$

where η is the viscosity of the grain boundary liquid and λ is the jump distance of the diffusion species, taken as the ionic diameter of an Al^{3+} (1.07 Å). Using viscosity data (range of 20 - 400 Pa*s) from the literature [22], we estimated the diffusion coefficients to be $\sim 1 \times 10^{-7}$ and $\sim 5 \times 10^{-9}$ cm 2 /s for $\text{Na}_2\text{O}/\text{SiO}_2$ co-doped and singly SiO_2 -doped samples, respectively.

Although we can calculate values for grain boundary thickness (δ) and viscosity (η), an exact α -ratio cannot be determined using Equation 2.3 because we do not know the interface reaction constant (K). Nevertheless, assuming a reasonable K value from the literature ($K = 5 \times 10^{-8}$ m/s) [19] and assuming that the A/B ratio (A and B being geometrical factors) is on the order of 1, we estimated α to be $\sim 10^{-2}$ and ~ 1 for singly SiO_2 -doped samples (603 ppm SiO_2) and $\text{Na}_2\text{O}/\text{SiO}_2$ co-doped samples (529/603 ppm), respectively. Thus, we conclude that at 1525°C densification of Bayer aluminas with low $\text{Na}_2\text{O}/\text{SiO}_2$ concentration ratios is governed by diffusion, whereas densification of Bayer aluminas with high $\text{Na}_2\text{O}/\text{SiO}_2$ concentration ratios can be governed by either diffusion or interface reaction.

The enhanced densification of $\text{Na}_2\text{O}/\text{SiO}_2$ co-doped samples compared to singly SiO_2 -doped is attributed to two factors; the increased solubility of Al_2O_3 in the liquid grain boundary phase, and the enhanced diffusion of Al^{3+} ($\sim 5 \times 10^{-9}$ to $\sim 1 \times 10^{-7}$ cm 2 /s) through the liquid grain boundary. This effect of enhanced densification of $\text{Na}_2\text{O}/\text{SiO}_2$ co-doped samples compared to singly SiO_2 -doped samples is observed in both the dilatometry curves and the densification kinetics data shown in Figure 2.2 and Figure 2.6, respectively.

It should be noted that a particular challenge for thermal processing studies with soda-based ceramics is Na_2O volatilization at relatively lower temperature than the sintering temperature. Soda by itself is highly volatile at temperatures

< 1000°C and the evaporation of soda from Na₂O containing technical ceramics such as sodium niobates [23] and β -Al₂O₃ during sintering is often reported. For example, β -Al₂O₃ (Na₂O·11Al₂O₃) has an appreciable Na₂O vapor pressure at temperatures > 1400°C [15], and when heated in air to > 1500°C, β -Al₂O₃ converts to α -Al₂O₃ by volatilization of Na₂O [15, 24]. Therefore, Na₂O evaporation from the samples during heating should be considered as samples might have somewhat lower Na₂O concentrations than assumed for the above calculations. Thus, for samples with low Na₂O:SiO₂ ratios, the liquid grain boundary phase may contain somewhat less Na₂O and the grain boundary thickness may be somewhat less than calculated. However, for singly Na₂O-doped samples and for co-doped samples with high Na₂O:SiO₂ ratios (e.g. Na₂O \geq 529 ppm for samples with 603 ppm SiO₂) the composition of the grain boundary liquid and the grain boundary thickness is not expected to change very much if Na₂O volatilizes. Consequently, even with Na₂O volatilization, the proposed sintering mechanisms do not change. The evaporation of Na₂O from Bayer Al₂O₃ samples will be further discussed in future work.

2.5 Summary

High concentrations of Na₂O in Bayer process Al₂O₃ powders inhibit densification in the initial sintering stage and retard densification up to the final sintering stage compared to powders with low Na₂O concentrations. However, Na₂O shows no adverse effect on the final density after longer hold times (\geq 3 h at 1525°C). The addition of SiO₂ to Bayer process Al₂O₃ powders substantially retards densification, starting at \sim 1250°C, and samples containing as much as 603 ppm SiO₂ are 4% less dense than samples containing 103 ppm SiO₂, even after hold times as long as 8 h at 1525°C. Co-doping with Na₂O and SiO₂ increases densification by 1 - 2.5% relative density relative to singly SiO₂-doped samples. The observed differences in sintering behavior can be explained by a liquid phase sintering model. Diffusion and solubility of Al₂O₃ in the SiO₂-based liquid in the grain boundaries is low at the temperatures used in this study, which explains the substantial retardation of densification by SiO₂. As predicted from the phase diagram Na₂O increases the solubility of Al₂O₃ in the siliceous grain boundary phase. As predicted from viscosity data Na₂O enhances diffusion of Al³⁺ through the liquid grain boundary phase. Both factors contribute to the enhanced densification rates of samples with

high $\text{Na}_2\text{O}/\text{SiO}_2$ ratios compared to samples with low $\text{Na}_2\text{O}/\text{SiO}_2$ ratios.

Table 2.1. Physical and chemical characteristics of the as-received Bayer Al₂O₃ powder used in this study.

BET (m ² /g)	7.4
D ₅₀ (μm)	0.4
D ₉₀ (μm)	1.5
	ICP (ppm)
Al ₂ O ₃	99.96 %
SiO ₂	103
Na ₂ O (total)	29
Fe ₂ O ₃	90
CaO	62
TiO ₂	22
MgO	2

Table 2.2. Calculated compositions and amounts of liquid in as-received, singly doped and co-doped samples at 1525°C ($\alpha = \alpha\text{-Al}_2\text{O}_3$, $\beta = \beta\text{-Al}_2\text{O}_3$, L= liquid, M = mullite).

Global dopant concentration		Global Na ₂ O:SiO ₂ ratio	Na ₂ O:SiO ₂ ratio in Liquid	Composition of liquid (mol %)			Amount of liquid (vol. %)	Stable phases
ppm (wt.)	ppm (mol)			Na ₂ O	SiO ₂	Al ₂ O ₃		
Na ₂ O/SiO ₂	Na ₂ O/SiO ₂							
As-received								
29/103	48/175	0.27	0.25	17.9	63.4	19.7	0.03%	$\alpha + L$
154/103-	253/175-							
1029/103	1693/175	1.45-9.67	0.5	26.1	52.3	21.6	0.03%	$\alpha + L + \beta$
29/603	48/1023	0.05	0.25	16.3	65.3	18.4	0.03%	$\alpha + L + M$
154/603	253/1023	0.25	0.25	16.3	65.3	18.4	0.16%	$\alpha + L$
279/603	459/1023	0.45	0.45	24.5	54.6	20.8	0.19%	$\alpha + L$
529/603	870/1023	0.85	0.5	26.1	52.3	21.6	0.22%	$\alpha + L + \beta$
1029/603	1693/1023	1.65	0.5	26.1	52.3	21.6	0.22%	$\alpha + L + \beta$

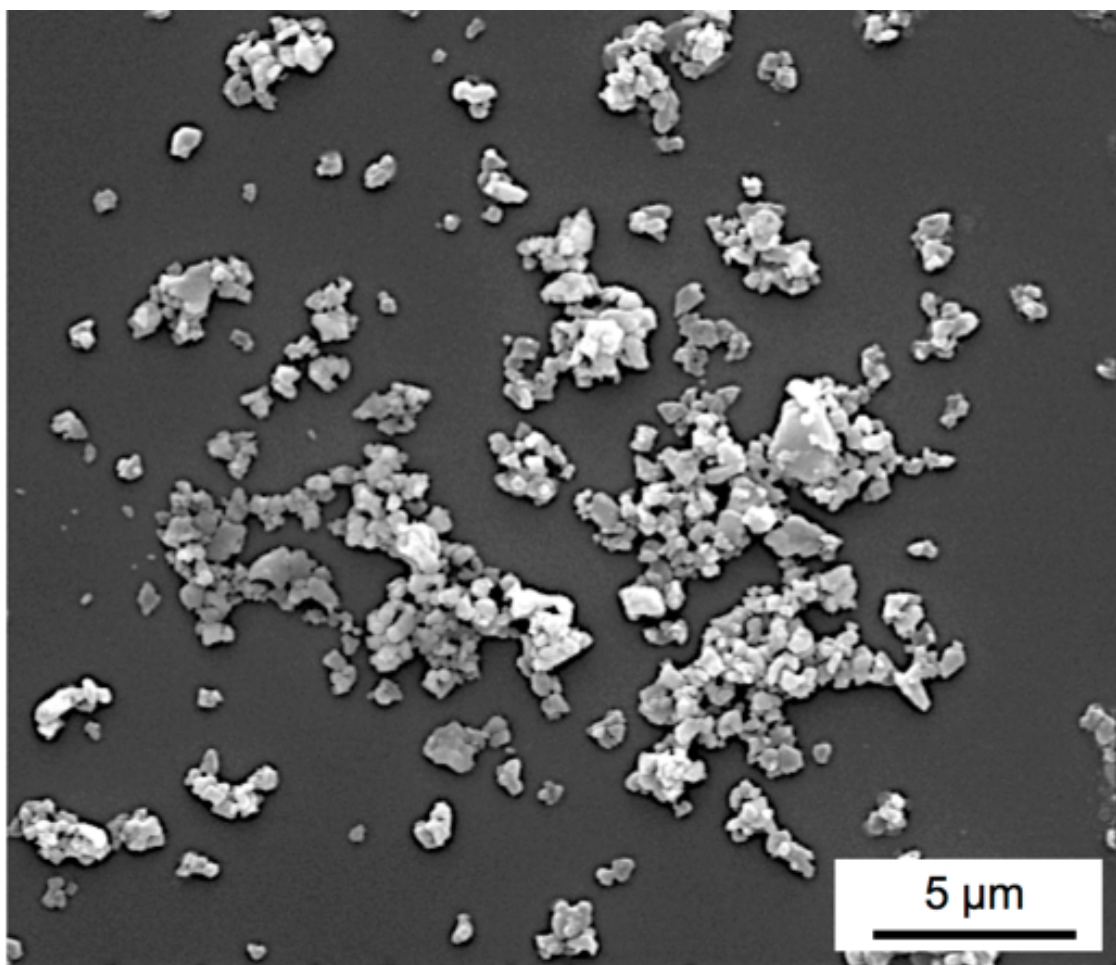


Figure 2.1. SEM image of as-received chemically purified Bayer Al_2O_3 powder used in this study.

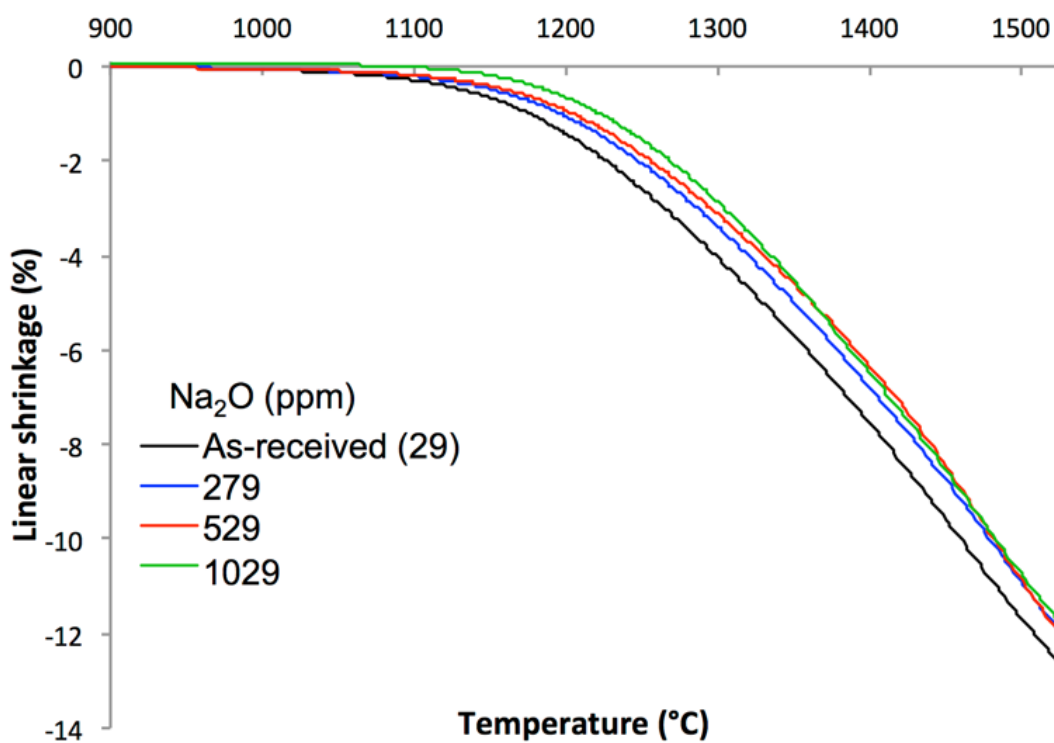


Figure 2.2. Dilatometer curves of as-received and singly Na_2O -doped samples heated at $10^{\circ}\text{C}/\text{min}$ to 1525°C .

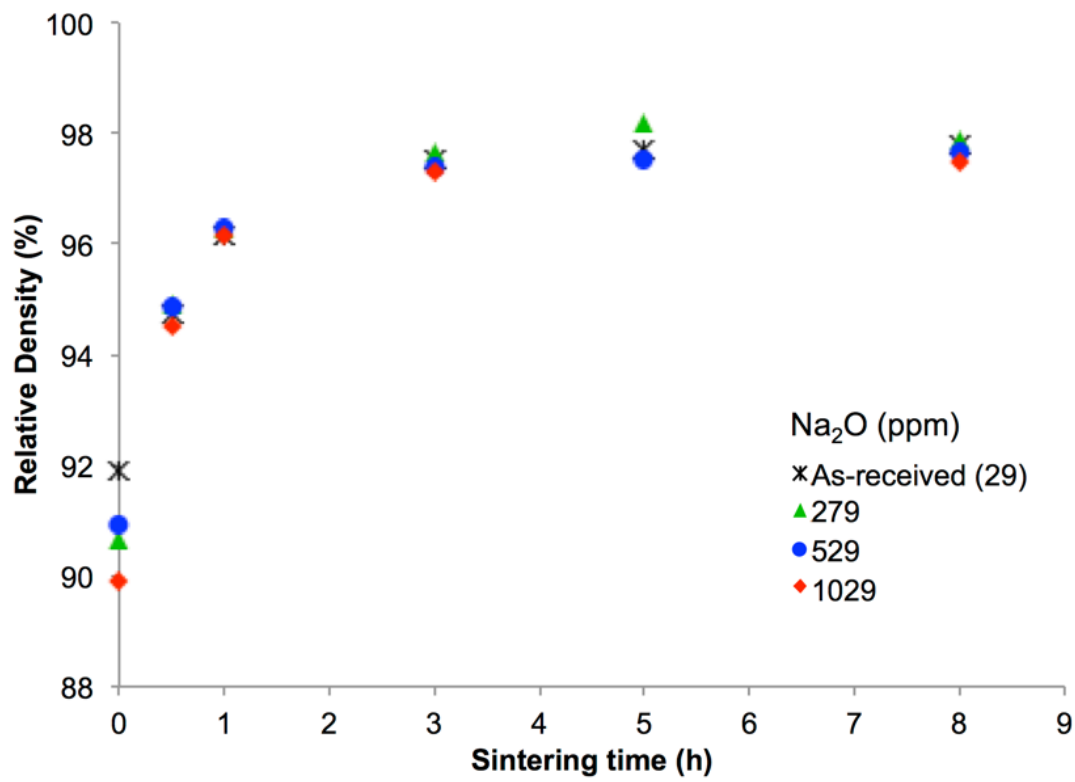


Figure 2.3. Densification kinetics of Bayer Al_2O_3 doped with different Na_2O concentrations and sintered at 1525°C .

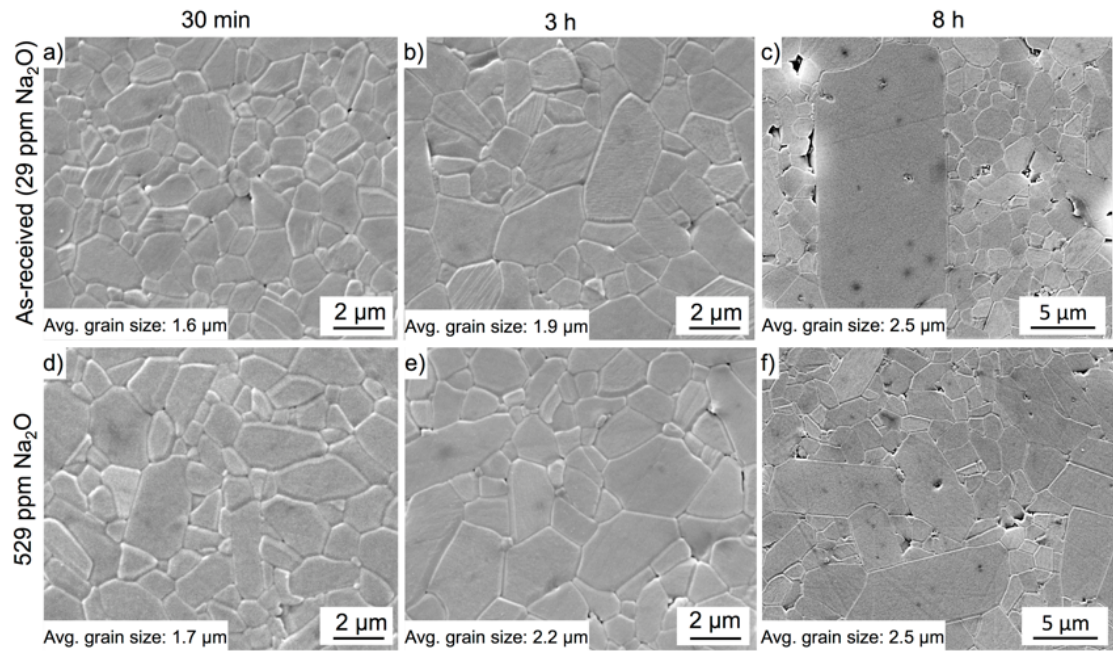


Figure 2.4. Microstructures of as-received and singly 529 ppm Na₂O doped samples after 30 min, 3 h and 8 h at 1525°C.

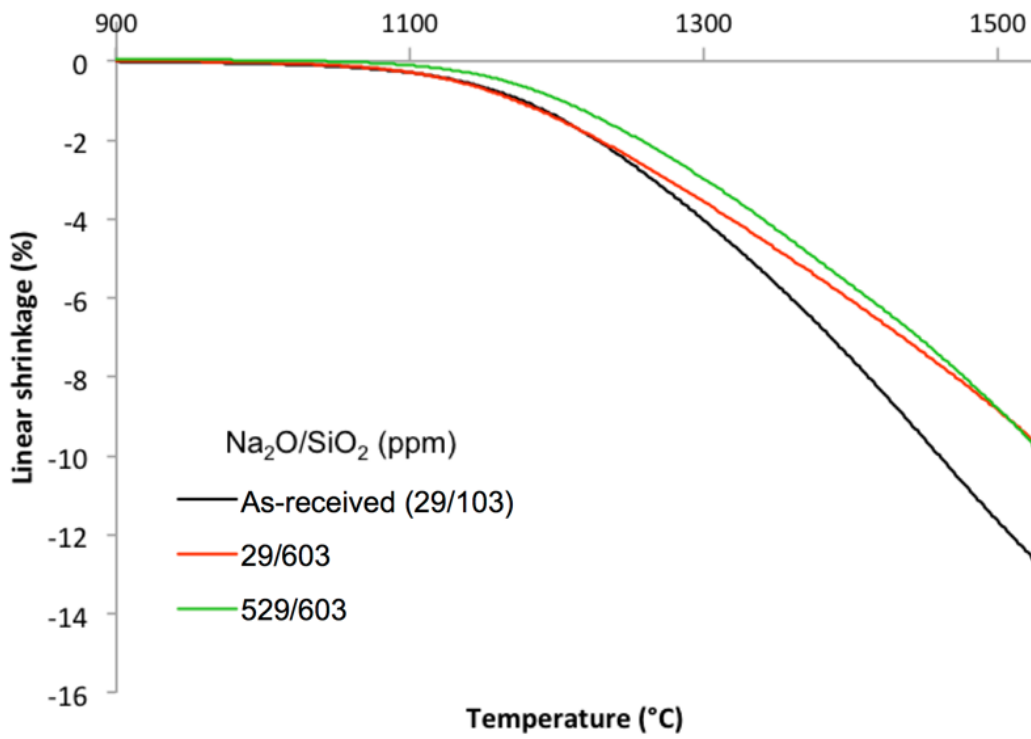


Figure 2.5. Dilatometer curves of as-received, singly SiO₂-doped, and Na₂O/SiO₂-doped Bayer Al₂O₃ heated at 10°C/min to 1525°C.

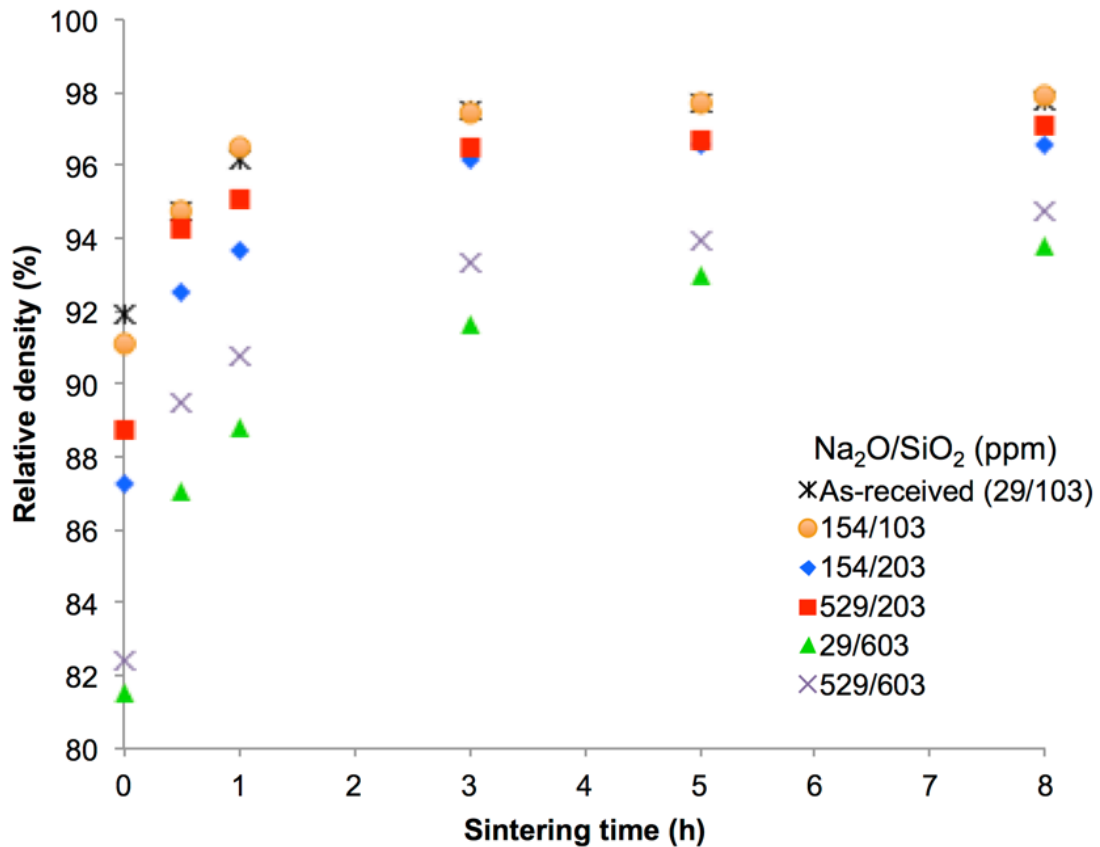


Figure 2.6. Densification kinetics of Bayer Al_2O_3 doped with different concentrations of Na_2O and SiO_2 at 1525°C .

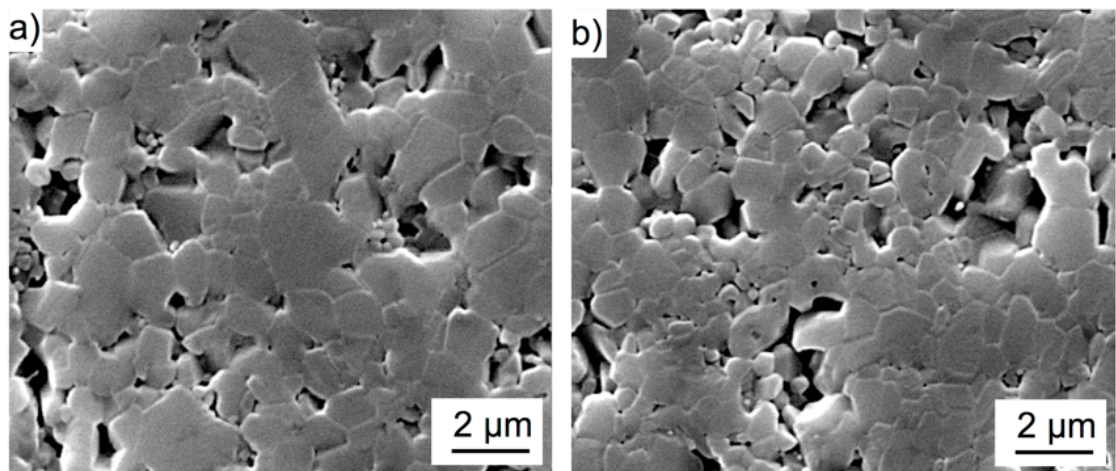


Figure 2.7. Microstructures of Bayer Al_2O_3 doped with a) 603 ppm SiO_2 and b) 529 ppm Na_2O and 603 ppm SiO_2 after heating at 1525°C for 8h.

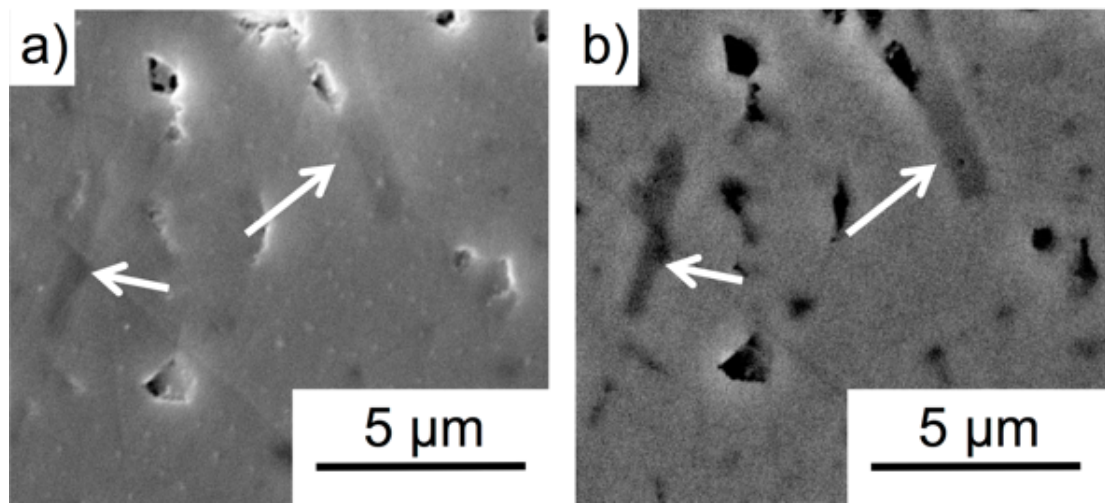


Figure 2.8. Micrographs of a sample doped with 1029 ppm Na_2O after sintering at 1525°C for 3 Åh. The micrographs were recorded using a) a secondary electron detector and b) a backscattered electron detector. The arrows point at the platelet shaped beta alumina grains that form in samples doped with Na_2O . The samples were not thermally etched.

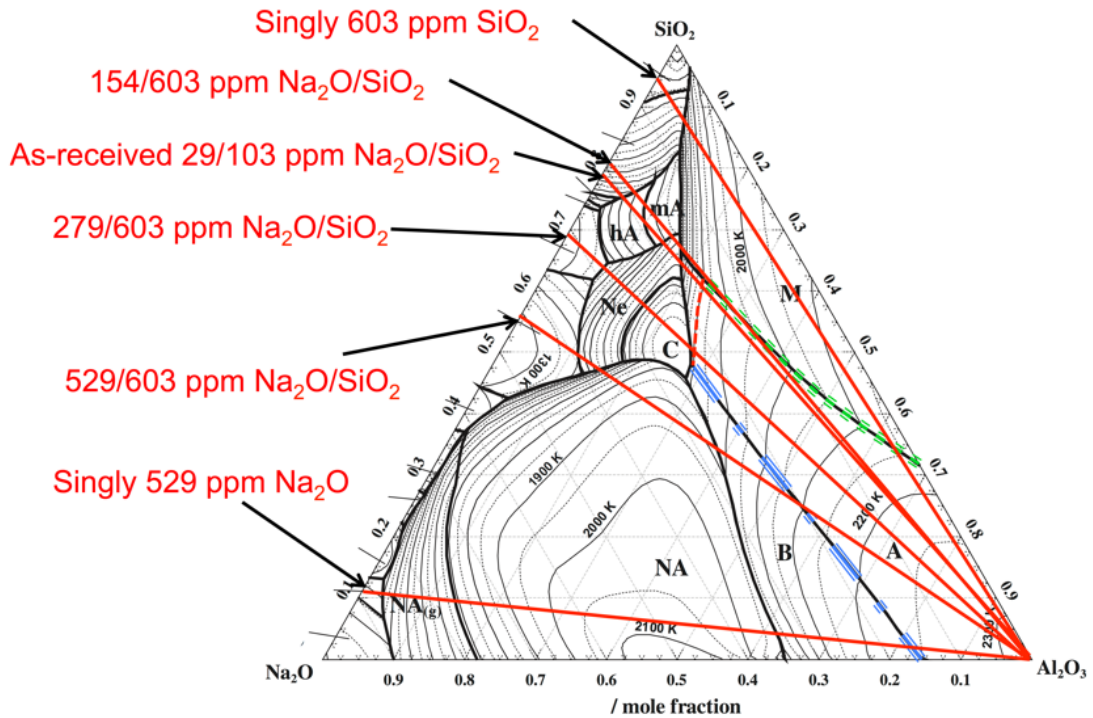


Figure 2.9. Liquidus projection of the Al_2O_3 - SiO_2 - Na_2O ternary phase diagram. The red solid lines are isoplethal cuts representing the samples investigated in this study. The red dashed line is the 1525°C isotherm where $\alpha\text{-Al}_2\text{O}_3$ and liquid are in equilibrium. The blue dash-dot line and green dotted line are eutectic lines at which $\alpha\text{-Al}_2\text{O}_3$ and liquid is in equilibrium with $\beta\text{-Al}_2\text{O}_3$ or mullite, respectively.

Chapter 3 | Powder Chemistry Effects on the Sintering Behavior of MgO- doped Bayer Alumina

3.1 Introduction

Specialty aluminas are generally defined as a calcined or sintered alumina made from a Bayer processed feedstock. These aluminas have specific characteristics to improve their performance in commercial applications, such as defined primary crystal size, surface area, density and shrinkage, and chemical purities in the range of 99.0 - 99.8%. The remaining 1.0 - 0.2% consists of the intentionally added MgO dopant, and impurities such as Na₂O, CaO, Fe₂O₃, and SiO₂ that originate from the bauxite ore or the Bayer process itself. It is well known that trace (ppm) amounts of dopants or impurities can have a significant influence on the sintering of alumina [1, 25, 26]. Since Coble's discovery of MgO doping to produce high-density translucent alumina, there has been high academic and commercial interest in understanding how small concentrations of dopants and impurities characteristic of specialty alumina affect sintering [2, 27–30].

In chapter 2, the influence of Na₂O and SiO₂ on the sintering of MgO-free specialty alumina was investigated [31]. Na₂O was shown to initially retard the densification of MgO-free specialty alumina samples, but no effect was observed after extended sintering time (> 30 min) at 1525°C, whereas the addition of SiO₂ to MgO-free specialty alumina formed a liquid phase and significantly retarded

densification throughout the entire sintering process. Na_2O addition to SiO_2 -doped samples increased the densification rate and degree of densification compared to singly SiO_2 -doped samples. Based on phase equilibria, the solubility of Al_2O_3 in the liquid phase was shown to increase as the Na_2O concentration in the liquid grain boundary phase increases. Furthermore, a higher Na_2O concentration decreases the viscosity of the liquid phase, which further increases the densification rate. Hence, samples with high $\text{Na}_2\text{O}/\text{SiO}_2$ ratios (≥ 0.5) showed higher densities than samples with lower $\text{Na}_2\text{O}/\text{SiO}_2$ ratios.

MgO is commonly added to commercial alumina powders because it is known to improve sintering. Several reasonable mechanistic explanations for the beneficial effect of MgO include solute-drag, particle-pinning, modification of defect chemistry, increase of surface diffusivity, modification of a liquid phase, and modification of interfacial properties [25]. A model that takes into account the redistribution of MgO and SiO_2 during the sintering of high purity alumina was reported by Handwerker et al. [32] They proposed that MgO changes the segregation behavior of glass forming impurities such as SiO_2 by increasing their solubility in Al_2O_3 . This mechanism was supported by the work of Gavrilov et al. [33] who demonstrated by high resolution secondary ion mass spectrometry that the dopants segregate strongly to grain boundaries when high purity Al_2O_3 is singly doped with either SiO_2 or MgO , but show a higher solubility in Al_2O_3 when co-doped with MgO and SiO_2 due to a defect mechanism in which Mg^{2+} and Si^{4+} occupy Al^{3+} sites and compensate for each other's charge and strain. This model is of particular interest since it considers the direct interaction of MgO and SiO_2 ; an impurity known to negatively affect alumina densification.

In this chapter we report how Na_2O and SiO_2 influence the sintering of 99.8 - 99.9% pure specialty alumina doped with 380 ppm MgO . Dilatometry and sintering kinetics of MgO -free specialty alumina samples with similar Na_2O and SiO_2 concentrations from chapter 2 are compared to the present results to identify the stages at which MgO affects densification, and to identify key mechanisms that are responsible for the beneficial effect of MgO on the sintering of specialty alumina [31]. High-resolution transmission electron microscopy (TEM) and energy dispersive spectroscopy (EDS) measurements show the distribution of dopants/impurities on grain boundaries. First-principles calculations based on the density functional theory (DFT) were carried out to estimate the relative thermodynamic stability of

MgO, SiO₂, and MgO+SiO₂ in the alumina lattice.

3.2 Experimental

A chemically purified MgO-doped specialty alumina powder (Almatis, Inc., Leetsdale, PA, USA) was chosen for this study. Earlier we studied the influence of SiO₂ and Na₂O on the sintering of MgO-free specialty alumina using a powder with similar physical and chemical characteristics as the powder used in this study [31]. Since the sample preparation procedures of the two powders were identical, the differences in sintering behavior after doping with similar Na₂O and SiO₂ concentrations should be attributable primarily to the difference in MgO concentration and its cross effects with Na₂O and SiO₂ [31].

Physical and chemical characteristics of the powder are shown in Table 3.1 and Figure 3.1. The powder was doped with up to 1000 ppm Na₂O and 500 ppm SiO₂ using sodium acetate (NaC₂H₃O_{2.3}H₂O, ACS grade, BDH, VWR International LLC, West Chester, PA, USA) and tetraethyl orthosilicate (Si(OC₂H₅)₄), 98%, Aldrich Chemical Company, Inc. Milwaukee, WI, USA), respectively, to obtain chemistries similar to commercial high purity specialty aluminas with different liquid volume fractions and different Na₂O/SiO₂ ratios, as shown in Table 3.2. The detailed doping procedures are described in chapter 2.

Samples with green densities of 59.0 ± 0.5% were fabricated for sintering studies by uniaxial and cold isostatic dry pressing (CIP, Autoclave engineers, Erie, Pa, USA) at 170 MPa and 200 MPa, respectively. The dry pressed cylinders were heated at 10 °C/min to 1525 °C in a thermomechanical analyzer (TMA, Linseis PT1600, Robbinsville, NJ, USA) to record the shrinkage during heating. The kinetics of sintering of samples at 1450 °C and 1525 °C were investigated for up to 8 h. The samples were heated at 10 °C/min to 1200 °C and then at 5 °C/min to the final sintering temperature. The average grain size and density were measured by the linear intercept (ASTM Standard E112-96) [4] and Archimedes methods (ASTM standard B962-15), [3] respectively. The structure and chemistry of grain boundaries were investigated by transmission electron microscopy (TEM) and energy dispersive x-ray spectroscopy EDS using a dual aberration corrected FEI Titan [26] field emission microscope operated at 300 kV and FEI Talos (FEI, Hillsboro, OR, USA) field emission microscope at 200 kV. The EDS on both microscopes is an FEI

Super-X system consisting of four SDDs (Silicon Drift Detectors) with a solid angle of 0.9 srad. The samples for TEM and EDS were air-quenched from the sintering temperature and prepared using a focused ion beam (Quanta 200 3D Dual Beam FIB, FEI, Hillsboro, OR, USA). Grain boundaries were chosen for analysis that were oriented parallel to the TEM beam in order to accurately measure grain boundary widths in the 2D projection images and EDS profiles. Chemical analyses were performed by inductively coupled plasma (ICP) emission spectroscopy (iCap 6000, Thermo Fischer Scientific, Inc., Waltham, MA, USA) after alumina samples were acid digested in a microwave digestion unit equipped with a Teflon sample holder (MARS M, CEM Corp., Matthews, NC, USA).

3.3 Computational Methodology

DFT-based first-principles calculations were carried out at 0 K to investigate the thermodynamic stability of clustered defects in the α -alumina structure. The energy at 0 K without the contribution of the zero-point vibrational energy E_0 was obtained by an equation of state (EOS) fitting using the four-parameter Birch-Murnaghan (BM4) equation as follows [34]:

$$E_0(V) = a + bV^{-\frac{2}{3}} + cV^{-\frac{4}{3}} + dV^{-2} \quad (3.1)$$

where a , b , c , and d are fitting parameters. The EOS fitting is achieved through an energy-volume (E-V) curve of at least 5 different volumes based on the methodology discussed by Shang et al. [34]. The Helmholtz energy $F(V, T)$ can be predicted as a function of temperature T and volume V via [34,35]:

$$F(V, T) = E_0(V) + F_{vib}(V, T) + F_{T-el}(V, T) \quad (3.2)$$

where F_{vib} is the temperature-dependent vibrational contribution, and F_{T-el} is the thermal electronic contribution. At ambient pressure, the Helmholtz energy of the system is equal to the Gibbs energy.

The vibrational contribution was obtained using the Debye-Grüneisen model [34]:

$$F_{vib}(V, T) = \frac{9}{8}k_B\theta_D(V) - k_BT \left[D \left(\frac{\theta_D(V)}{T} \right) + 3\ln \left(1 - e^{-\theta_D(V)/T} \right) \right] \quad (3.3)$$

where θ_D is the Debye temperature, T the temperature, and $D[\theta_D(V)/T]$ the Debye function. The Debye temperature can be calculated by:

$$\theta_D = s \frac{(6\pi^2)^{\frac{1}{3}} \hbar}{k_B} V_0^{\frac{1}{6}} \left(\frac{B_0}{M} \right)^{\frac{1}{2}} \left(\frac{V_0}{V} \right)^\gamma \quad (3.4)$$

where s is the Debye temperature scaling factor, γ the Grüneisen parameter determined by the pressure derivative of bulk modulus B' , B_0 the equilibrium bulk modulus, M the atomic mass, and V_0 the equilibrium volume. Here, the equilibrium properties V_0 , B_0 , and B' are estimated from the EOS of Eq. 3.1. The methodology by Liu et al. [36] was used to calculate the scaling factor of Al_2O_3 :

$$s(\nu) = 3^{\frac{5}{6}} \left(4\sqrt{2} \left(\frac{1+\nu}{1-\nu} \right)^{\frac{3}{2}} + \left(\frac{1+\nu}{1-\nu} \right)^{\frac{3}{2}} \right)^{-\frac{1}{3}} \quad (3.5)$$

where ν is the Poisson's ratio, which was calculated by Shang et al. [37]. The thermal electronic contribution was estimated based on the electronic density of states and the Fermi-Dirac statistics [35].

In the present work, the Vienna Ab-initio Simulation Package (VASP) was used to perform the first-principles calculations [38]. The projector augmented-wave (PAW) [39, 40] method was utilized to describe the electron-ion interactions with the exchange correlation functional given by the generalized gradient approximation (GGA-PW91) [41]. A sigma value of 0.2 eV and a plane wave energy cutoff of 1.3 times higher than the highest default cutoff were adopted. The Brillouin zone sampling was carried out with Blöchl corrections using a gamma centered Monkhorst-Pack (MP) scheme [40, 42]. The automated k-points grid generator in VASP was employed with a subdivision length of 80. The energy convergence criterion of the electronic self-consistency was set at 10^{-5} eV/atom for all calculations.

The energies of charge, site, and mass balanced defects in α -alumina were calculated for defect clusters, i.e. the defects are located next to each other, since this has been shown to be the most stable configuration [43]. The geometric arrangements of each of the clusters were chosen based on previous computational work. Multiple authors showed that a 30-40 atom supercell of Al_2O_3 is sufficient to calculate non-charged defects [43–47]. Multiple authors have studied charged and clustered defects in Al_2O_3 [43–47]. They showed that different geometric arrangements and supercell size result in little difference in energy and that the

impurity atoms prefer to be clustered due to the binding energy [43–47]. Using this methodology, supercells were generated in the present work with Mg and/or Si clustered, i.e. the Mg-cluster having two Mg atoms substituted for two Al atoms and an oxygen vacancy as nearest neighbors, the Si-cluster having three Si atoms substituted for three Al atoms and an Al vacancy, and the Mg+Si-cluster having one Mg and one Si substituted for two Al atoms.

3.4 Sintering and Microstructure Analysis

In chapter 2, it was shown that a glass phase can form during sintering of specialty alumina. Table 3.2 shows the amounts of liquid in the samples at 1525 °C estimated from the $\text{Al}_2\text{O}_3\text{-Na}_2\text{O}\text{-SiO}_2$ and $\text{Al}_2\text{O}_3\text{-MgO}\text{-SiO}_2$ phase diagrams based on the amount of SiO_2 , Na_2O and MgO [48]. It can be seen that the glass volume fraction increases from 0.03 vol.% for SiO_2 concentrations of 82 ppm to 0.21 vol.% for SiO_2 concentrations of 582 ppm at 1525 °C.

Figure 3.2 shows the dilatometry curves of MgO-doped and MgO-free [31] samples with different Na_2O and SiO_2 concentrations heated at 10 °C/min to 1525°C. For samples with SiO_2 concentrations of 582 ppm the estimated amount of liquid increases from 0.18 vol.% to 0.21 vol.% during heating from 1250 °C to 1525 °C, and for samples with 82 ppm SiO_2 the amount of liquid phase is estimated from the phase diagram to increase from 0.026 vol.% to 0.030 vol.% during heating from 1250 °C to 1525 °C.

Figure 3.2a shows that the onset of densification of MgO-doped specialty alumina is shifted to higher temperatures for samples with higher Na_2O concentrations. Samples with 560 ppm Na_2O shrink 1% less than samples with 60 ppm Na_2O after heating to 1525 °C. In both the MgO-doped and the MgO-free powders, higher SiO_2 concentrations retard densification at ~1250 °C. However, the retardation caused by higher SiO_2 concentrations is less severe in the MgO-doped powder than in the MgO-free powder; e.g. already at 1300 °C, MgO-doped powder samples with 582 ppm SiO_2 (after the addition of 500 ppm SiO_2) shrink 0.2% less and are 0.5% less dense than samples with 82 ppm SiO_2 , whereas samples of the MgO-free powder with 603 ppm SiO_2 shrink 0.5% less and are 3.2% less dense than samples with 103 ppm SiO_2 . After reaching 1525 °C the dilatometry curves show that MgO-doped samples with 582 ppm SiO_2 (0.21 vol.% glass) shrink 1.8% less and

are 5.4% less dense than MgO-doped samples with 82 ppm SiO₂ (0.03 vol.% glass). In contrast, the retardation of densification caused by the addition of 500 ppm SiO₂ to the MgO-free powder results in 3.0% less linear shrinkage and 8.7% lower relative densities after heating to 1525 °C. MgO-doped (380 ppm) powder samples with 560 ppm Na₂O and 582 ppm SiO₂ shrink ~2.5% less than samples with 60 ppm Na₂O and 82 ppm SiO₂ after reaching 1525 °C, and MgO-free powder samples with 529 ppm Na₂O and 603 ppm SiO₂ shrink ~3.0% less than samples with 29 ppm Na₂O and 103 ppm SiO₂ after reaching 1525 °C.

Figure 3.3a and b show how the sintering kinetics of MgO-doped and MgO-free [31] alumina are affected by Na₂O and SiO₂ after heating at 1450 °C and 1525 °C for up to 8 h. The density of samples with higher SiO₂ concentrations, i.e. higher glass concentrations, is lower for all hold times at 1450 °C and 1525 °C. At 1450 °C MgO-doped powder samples with 0.19 vol.% glass phase (582 ppm SiO₂) are 6-7% less dense than samples with 0.027 vol.% glass phase (82 ppm SiO₂), for all hold times (Figure 3.3a). At 1525 °C MgO-doped powder samples with 0.21 vol.% glass phase are ~11% and ~2% less dense than samples with 0.03 vol.% glass phase after heating for 0 h and 8 h, respectively, and samples with 0.03 vol.% glass phase reach densities >98% after 1 h, whereas samples with 0.066 and 0.21 vol.% glass phase are only ~96% and ~94% dense, respectively (Figure 3.3b).

The effect of Na₂O concentration on densification strongly depends on glass phase concentration. In all samples a higher Na₂O concentration initially retards densification. For example, after 0 h at 1450 °C the relative density of samples with 0.03 vol.% glass phase and 560 ppm Na₂O is ~3% lower than the relative density of samples containing the same amount of glass phase and 60 ppm Na₂O. However, there is no difference in sintered density after 3 h at either 1450 °C or 1525 °C. For samples with higher glass phase concentrations (e.g., 0.21 vol.%) the effect of Na₂O on the densification is not straightforward, due to the changing Na₂O/SiO₂ ratio from 0.1 to 0.9 (Table 3.2). Samples with 0.21 vol.% glass phase and Na₂O/SiO₂ ratios of 0.9 are 1-2% denser than samples with 0.21 vol.% glass phase and Na₂O/SiO₂ ratios of 0.1. However, after 30 min at 1525 °C the relative density of samples with 0.21 vol.% glass phase and Na₂O/SiO₂ ratios of 0.9 in the glass phase is 0.9% lower than the relative density of samples with 0.21 vol.% glass phase and Na₂O/SiO₂ ratios of 0.1 in the glass phase, and after 1 h or longer at 1525 °C there is no difference in relative density. Samples with 0.066 vol.% glass

phase are 98.3 - 98.6% dense after 8 h at 1525 °C, and samples with 0.21 vol.% glass phase are 97.1% - 97.5% dense after 8 h at 1525 °C.

Comparing the as-received MgO-free and MgO-doped powders with 0.03 vol.% glass phase shows that doping with 380 ppm MgO leads to 1% higher densities for all hold times at 1525 °C (Figure 3.3b and c) [31]. After 8 h at 1525 °C the MgO-doped samples with 0.21 vol.% glass phase are ~2% less dense than samples with 0.03 vol.% glass phase, whereas the addition of 500 ppm SiO₂ (total of 603 ppm SiO₂ and 0.22 vol.% glass) to the MgO-free powder leads to ~4% less dense samples [31]. MgO-free and MgO-doped specialty alumina samples containing 0.22 and 0.21 vol.% glass phase, respectively, and global Na₂O/SiO₂ ratios of 0.9 show initial retardation of densification compared to samples with Na₂O/SiO₂ ratios of 0.1, but have higher densities than samples with Na₂O/SiO₂ ratios of 0.1 after further heating. This increased densification can be explained by the increased solubility of Al₂O₃ into the liquid grain boundary phase and the higher diffusivity (lower viscosity of the grain boundary phase) as the Na₂O/SiO₂ ratio increases [19, 31]. However, after hold times of 1 h or longer at 1525 °C, MgO-free powder samples with 0.22 vol.% glass phase and Na₂O/SiO₂ ratios of 0.9 are 1% denser than samples with 0.22 vol.% glass phase and Na₂O/SiO₂ ratios of 0.1, whereas MgO-doped powder samples with 0.21 vol.% and Na₂O/SiO₂ ratios of 0.9 have the same densities as samples with 0.21 vol.% glass phase and Na₂O/SiO₂ ratios of 0.1.

The microstructures of samples with different vol.% glass phase and different Na₂O/SiO₂ ratios heated at 1525 °C for 8 h are shown in Figure 3.4. Samples with 60 ppm Na₂O show mostly equiaxed grains, regardless of the glass phase concentration in the samples (Figures 3.4a and c). Samples with 560 ppm Na₂O (Figures 3.4b and d) show more faceted α-Al₂O₃ grains and appear to have a wider grain size distribution than samples with 60 ppm Na₂O. These effects are more pronounced in samples with higher glass concentrations. The grain sizes of samples with 0.21 vol.% glass are less than the grain sizes of samples with 0.03 vol.% glass phase.

The average grain sizes of samples with different vol.% glass phase and different Na₂O/SiO₂ ratios are plotted as a function of relative density in Figure 3.5. Grain growth starts when the final sintering stage is reached, between 85 and 92% relative density. Samples with 0.03 vol.% glass phase and 60 ppm Na₂O show a three-fold

increase in grain size, from $0.5 \mu\text{m}$ to $\sim 1.5 \mu\text{m}$, when the relative density increases from 68% to 99%, and samples with 0.03 vol.% glass phase and 560 ppm Na_2O have a somewhat larger grain size of $2.2 \mu\text{m}$ at 99% relative density. When relative densities of $\sim 99\%$ are reached in samples with 0.03 vol.% glass, the grain size increases to $3.1 - 3.4 \mu\text{m}$ when heated at 1525°C for 8 h. Samples with higher glass concentrations have a similar trajectory up to 92% density. However, at densities $>92\%$ grain growth is enhanced in samples with higher glass concentrations, and at 97 - 97.5% density higher glass phase concentrations of 0.21 and 0.17 vol.% lead to a larger grain size of 2.6 and $2.4 \mu\text{m}$, respectively, compared to samples with 0.03 vol.% glass phase ($\sim 1.5 \mu\text{m}$ grain size).

3.5 Mechanistic Interpretation

If the mechanism of MgO increasing the solubility of SiO_2 in alumina, as proposed by Handwerker et al., [32] is responsible for the improved sintering behavior of alumina, then the amount of liquid phase in MgO -doped alumina should be less than calculated and less than in MgO -free samples, and, the grain boundary thickness in MgO -doped alumina should be less than in MgO -free powder. The reduced grain boundary thickness in MgO -doped alumina should lead to a change in grain boundary chemistry and different sintering behavior after this co-dissolution has occurred compared to MgO -free alumina.

Comparing the dilatometry curves and sintering kinetics of MgO -doped and MgO -free specialty alumina powders with different chemistries indicates that there are two stages at which MgO affects densification. At 1250°C increased glass phase content retards densification, and at the same stage there is an enhancement of densification due to MgO . This suggests that there is a direct interaction between the glass phase and MgO at this stage, where MgO mitigates the negative effect of the glass phase, probably by modifying the properties of the liquid grain boundary phase. The Al_2O_3 - SiO_2 - MgO phase diagram suggests that MgO increases the solubility of Al_2O_3 in the liquid, and MgO can lower the viscosity of the glass melt, [22] which results in higher diffusion coefficients. The enhanced diffusion associated with the lower viscosity and higher solubility of Al_2O_3 in the glass phase can explain why MgO positively affects the sintering of alumina at stages when SiO_2 would negatively affect densification.

The second stage at which MgO affects densification is after 1 h at 1525 °C. MgO-free powder samples with 0.22 vol.% glass phase and Na₂O/SiO₂ ratios of 0.9 have 1-2% higher relative densities than samples with 0.22 vol.% glass phase and Na₂O/SiO₂ ratios of 0.1 for all hold times at 1525 °C. In previous work we calculated an expected grain boundary thickness of 1.3 nm for samples with 0.22 vol.% glass phase after 3 h at 1525 °C, based on the observed grain size of 1.6 μm. The addition of 500 ppm Na₂O increases the Na₂O/SiO₂ ratio from 0.1 to 0.9, which modifies the liquid grain boundary phase and enhances densification [31]. Figure 3.6 shows a high-resolution TEM image of a grain boundary of a MgO-free powder [31] sample (2 ppm MgO) with 0.22 vol.% glass phase and a Na₂O/SiO₂ ratio of 0.9 after 3 h at 1525 °C. It can be seen that the measured grain boundary thickness of 1.7 nm is close to the grain boundary thickness calculated based on the amount of glass phase in the sample. MgO-doped powder samples with 0.21 vol.% glass phase and Na₂O/SiO₂ ratios of 0.9 have 1-2% higher densities than samples with 0.21 vol.% glass phase and Na₂O/SiO₂ ratios of 0.1 for most hold times at 1450 °C and for hold times < 30 min at 1525 °C. This difference in densification behavior is similar to the densification behavior of MgO-free powder samples, which suggests the presence of a liquid phase that is modified by Na₂O, as seen in the MgO-free alumina samples.

Figure 3.7a shows a high resolution TEM image of a grain boundary in an MgO-doped alumina sample with 0.21 vol.% glass phase and a Na₂O/SiO₂ ratio of 0.9 after 0 h at 1525 °C. The measured grain boundary thickness of ~1.4 nm for this sample is in agreement with the theoretically estimated [31] grain boundary thickness. However, after 1 h or longer at 1525 °C, samples with 0.21 vol.% glass and Na₂O/SiO₂ ratios of 0.9 have the same densities as samples with 0.21 vol.% glass and Na₂O/SiO₂ ratios of 0.1, and the grain boundary thicknesses of those samples after 3 h at 1525 °C are ~0.3 nm (Figure 2.7b) and substantially thinner than the calculated grain boundary thicknesses of 1.4 nm.

The thinner grain boundary suggests that the addition of MgO causes a reduction of the amount of liquid phase in the grain boundaries after longer time at 1525 °C. In the literature it is reported that excess liquid phase, after an equilibrium grain boundary thickness [49] is reached, can accumulate in triple pockets. However, we did not observe any triple pockets in the 380 ppm MgO-doped samples with 0.21 vol.% glass. Therefore, the impurities and dopants that formed the liquid

phase after 0 h have to be distributed elsewhere in the sample after 3 h at 1525 °C. Since SiO_2 -containing second phases, such as mullite or cordierite, were not observed in the samples, we hypothesize that SiO_2 and MgO form a solid solution in α -alumina, as proposed by Handwerker et al. [32]. This co-dissolution mechanism would significantly reduce the total amount of SiO_2 and, therefore, the liquid phase content in the samples and in the grain boundaries.

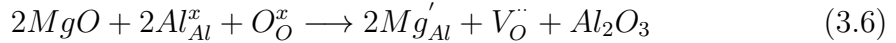
The EDS maps in Figure 2.8 show the distribution of Si around a grain boundary in MgO -doped samples with a calculated glass concentration of 0.21 vol.% after 0 h and 3 h at 1525 °C. Figure 2.9 shows the corresponding EDS line scans for Si and Mg across the grain boundaries. It can be seen that after 0 h at 1525 °C SiO_2 and MgO are strongly concentrated in the grain boundaries, and a chemical grain boundary thickness, δ_{chem} , of ~ 1.7 nm is estimated (Figures 2.8a and 2.9a), which is close to the structural grain boundary thickness of 1.4 nm measured from the high resolution TEM image (Figure 2.7a). After 3 h at 1525 °C MgO and SiO_2 are still concentrated on the grain boundary, however, the chemical grain boundary thickness, δ_{chem} , is ~ 3.2 nm (Figure 2.8b and 2.9b) and substantially thicker than the observed structural grain boundary thickness, δ_{str} , of ~ 0.3 nm (Figure 2.7b). This difference in structural and chemical grain boundary thickness after 3 h supports the argument that MgO and SiO_2 form a solid solution in the alumina lattice in the near grain boundary region. If we assume that equal amounts of MgO and SiO_2 dissolve into the alumina lattice to form the proposed defect complex, and that all MgO in the sample is consumed by this process, then 380 ppm SiO_2 must be removed from the amorphous grain boundary phase. This would leave 202 ppm SiO_2 in the grain boundaries to form the amorphous film with a calculated grain boundary thickness of 0.5 nm, which is close to the observed grain boundary thickness of 0.3 nm [31].

To further evaluate whether MgO and SiO_2 form a solid solution in α -alumina we conducted first-principles calculations based on density functional theory to gain insight into the thermodynamic stability of Mg^{2+} and Si^{4+} by themselves and together in the α -alumina structure. To ensure the accuracy of the calculations, the lattice parameters and energy of the α -alumina structure without any substitutions are compared with previous experiments and calculations in Table 3.3. It can be seen that the calculated lattice parameters match well with experimental values and lattice parameters from previous first-principles calculations [43, 50–54]. The

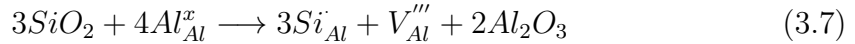
difference between the present and past first-principles calculations can be attributed to the different input parameters used.

We calculated the energy of a unit cell of the $\hat{\text{I}}$ -alumina structure with substitutions according to the following balanced equations:

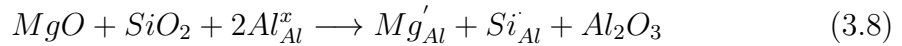
Mg-Cluster:



Si-Cluster:



Mg+Si-Cluster:



Defect simulations of aliovalent cation substitutions in alumina [43] showed that the dominant compensation mechanisms for Mg^{2+} and Si^{4+} by themselves in alumina are the formation of oxygen and aluminum vacancies, respectively (Eq.3.6 and 3.7). In Eq. 3.8 Mg^{2+} and Si^{4+} compensate for each other's charge and the formation of vacancies or interstitials is unnecessary to account for dissolution in the alumina lattice. The calculations were carried out for clustered defects since they are lower in energy than isolated defects [43]. The structures were relaxed and the formation energies as a function of temperature with bulk Al_2O_3 as the reference state are plotted in Figure 3.10. It can be seen that the formation energy for the Mg+Si-cluster, $E_{\text{Form}}^{\text{Mg+Si}}$, is lower than the formation energies of the Mg-cluster, $E_{\text{Form}}^{\text{Mg}}$, and the Si-cluster, $E_{\text{Form}}^{\text{Si}}$, which indicates that the Mg+Si-cluster is more stable than the Mg-cluster and the Si-cluster. Since two Mg^{2+} ions and three Si^{4+} ions are necessary to form the Mg-cluster and Si-cluster, respectively, but only one Mg^{2+} and one Si^{4+} are required to form the Mg+Si-cluster, the formation energies of the clusters can be compared by

$$\Delta E_{\text{Form}} = E_{\text{Form}}^{\text{Mg+Si}} - \left(\frac{1}{3}E_{\text{Form}}^{\text{Si}} + \frac{1}{2}E_{\text{Form}}^{\text{Mg}} \right) \quad (3.9)$$

The formation energy difference, ΔE_{Form} , is plotted in Figure 3.10 and it can be

seen that ΔE_{Form} is negative at all temperatures, which means that the Mg+Si-cluster is more energetically favored to form than the Mg-cluster or Si-cluster. This indicates that MgO and SiO₂ have a higher co-solubility in α -alumina than MgO or SiO₂ by themselves. In α -alumina the Al³⁺ cation sites are 6-fold coordinated and Al³⁺ has an effective ionic radius of 53.5 pm, while the radii of Mg²⁺ and Si⁴⁺ are 72 pm and 40 pm, respectively. Therefore, Mg²⁺ and Si⁴⁺ can compensate for each other's size and charge difference relative to Al³⁺ in the α -alumina lattice, which explains the lower energy of the Mg+Si-cluster. The stable phases for MgO and/or SiO₂ and Al₂O₃ are spinel, cordierite, and mullite. However, we hypothesize that if both MgO and SiO₂ are present at low concentrations, then it is more favorable for MgO and SiO₂ to form a solid solution in the α -alumina structure than to form a second phase or remain in the grain boundaries as a siliceous liquid phase.

The described mechanism could also influence the distribution of other oxides in the samples, such as Fe₂O₃, CaO, and Na₂O. Figure 3.11 shows the element distribution obtained from EDS of two grain boundaries in samples sintered at 1525 °C for 0 h and 3 h, respectively. Figures 3.11a and e show the segregation of MgO to the grain boundaries after 0 h and 3 h, respectively, and it can be seen that after 0 h at 1525 °C Mg is more strongly concentrated in the grain boundary than after 3 h at 1525 °C, due to the mechanism described above. From Figures 3.11b and f it can be seen that there is no segregation of Fe₂O₃ and we believe that Fe₂O₃ is in solid solution in the alumina lattice, [43] since the Al₂O₃-Fe₂O₃ phase diagram shows considerable solubility [55]. Figures 3.11c, d, g, and h show that there is a slightly higher Na and Ca signal coming from the grain boundaries, indicating that Na and Ca segregate to the grain boundaries and are components of the liquid grain boundary phase. Ca is more concentrated in the grain boundary after 3 h at 1525 °C, due to the narrower grain boundary thickness (Figure 3.7b).

It can be seen that the Na signal after 0 h at 1525 °C (Figure 3.11c) shows a slight segregation of Na to the grain boundary, but after 3 h at 1525 °C (Figure 3.11g) no segregation can be observed. It should also be noted that it is challenging to detect Na using EDS since the Na signal disappears quickly after the high-voltage electron beam is focused on the grain boundary. Therefore, we believe that there is still Na on the grain boundaries, even though the EDS map does not show an increased Na signal. However, since the Na signal is lower, we believe that after 3 h at 1525 °C there is less Na₂O on the grain boundaries than after 0 h at 1525 °C. The

reduced amount of Na might be a result of volatilization of Na_2O during sintering. Figure 3.12 shows the influence of sintering time and temperature on the Na_2O concentration, obtained by ICP analysis, during sintering for samples with target concentrations of 560 ppm Na_2O . It can be seen that there is no observable Na_2O loss as a function of temperature up to 1525 °C (Figure 3.12a), but after heating to 1600 °C there is a loss of ~200 ppm or a ~35% decrease in Na_2O concentration. After sintering at 1525 °C for 30 min the Na_2O concentration decreases by about 200 ppm, but remains constant at ~350 ppm when heated to 1525 °C for up to 8 h (Figure 3.12b). Between 1300 °C and 1525 °C the Na_2O concentration is constant at ~510 ppm, which is 50 ppm below the target level. The lower Na_2O concentration might be due to volatilization at earlier stages. During heating at 1525 °C Na_2O loss can be observed between 0 and 30 min hold time, which can explain the lower Na signal in Figure 3.11g.

As explained earlier, the described dissolution of MgO and SiO_2 into the alumina lattice reduces the amount of glass phase in the grain boundaries. Since only SiO_2 is removed from the glass phase and other components of the glass phase, such as CaO and Na_2O remain, the grain boundaries can supersaturate. This can eventually lead to the nucleation of second phases, which was observed for samples with lower SiO_2 concentrations of 82 and 182 ppm.

3.6 Summary and Conclusion

The effect of MgO on the sintering of specialty alumina powders with different chemistries was analyzed by comparing the sintering kinetics of MgO -free and MgO -doped specialty aluminas with different impurity levels and ratios of Na_2O and SiO_2 . TEM images of grain boundaries shows that the grain boundary thickness of MgO -doped specialty alumina is reduced during densification at 1525 °C and are thinner than observed in MgO -free specialty alumina. EDS analysis suggests that MgO and SiO_2 have an increased co-solubility in the alumina lattice when present together. This co-dissolution mechanism was supported by DFT-based first-principles calculations showing that the formation energy of MgO and SiO_2 together in the alumina lattice is lower than the formation energies of MgO or SiO_2 by themselves in the alumina lattice. The reduced amount of SiO_2 on the grain boundaries of MgO -doped alumina leads to enhanced densification compared to

MgO-free alumina because SiO_2 has been shown to retard densification.

The present study supports the hypothesis of Handwerker et al. [32] and high resolution SIMS observations of Gavrilov et al. [33] that the key mechanism responsible for the beneficial effect of MgO on the sintering of alumina is the reduction of amorphous phase in the grain boundaries by increasing the solubility of SiO_2 in the alumina lattice.

Table 3.1. Physical and chemical characteristics of the as-received 380 ppm MgO-doped specialty alumina powder used in this study.

BET (m^2/g)	7.3
D_{50} (μm)	0.4
D_{90} (μm)	1.4
	ICP (ppm)
Al_2O_3	99.92 %
SiO_2	82
Na_2O	60
Fe_2O_3	140
CaO	51
TiO_2	8
MgO	380

Table 3.2. Calculated compositions and amounts of liquid in 380 ppm MgO-doped specialty alumina samples of different chemistries at 1450°C and 1525 °C.

Na ₂ O/SiO ₂ concentration		Global Na ₂ O/SiO ₂ ratio	Na ₂ O:SiO ₂ ratio in the liquid	Vol. % of liquid in sample	
ppm by wt.	ppm by mole			1450 °C	1525 °C
60/82 - 560/82	99/139 - 921/139	0.7 - 6.6	0.5	0.027	0.030
185/182 - 560/182	304/309 - 921/309	1.0 - 3.0	0.5	0.060	0.066
60/582	99/987	0.1	0.1	0.19	0.21
560/582	921/987	0.9	0.5	0.19	0.21

Table 3.3. Lattice parameters and equilibrium energy (E_0) compared to previous first-principles and experimental values.

Reference	E_0 (eV/atom)	a (Å)	b (Å)	c (Å)
This work	-7.48	4.76	4.76	12.99
Calc [50–54]	-7.48	4.78	4.78	13.00
Expt [43]		4.76	4.76	13.00

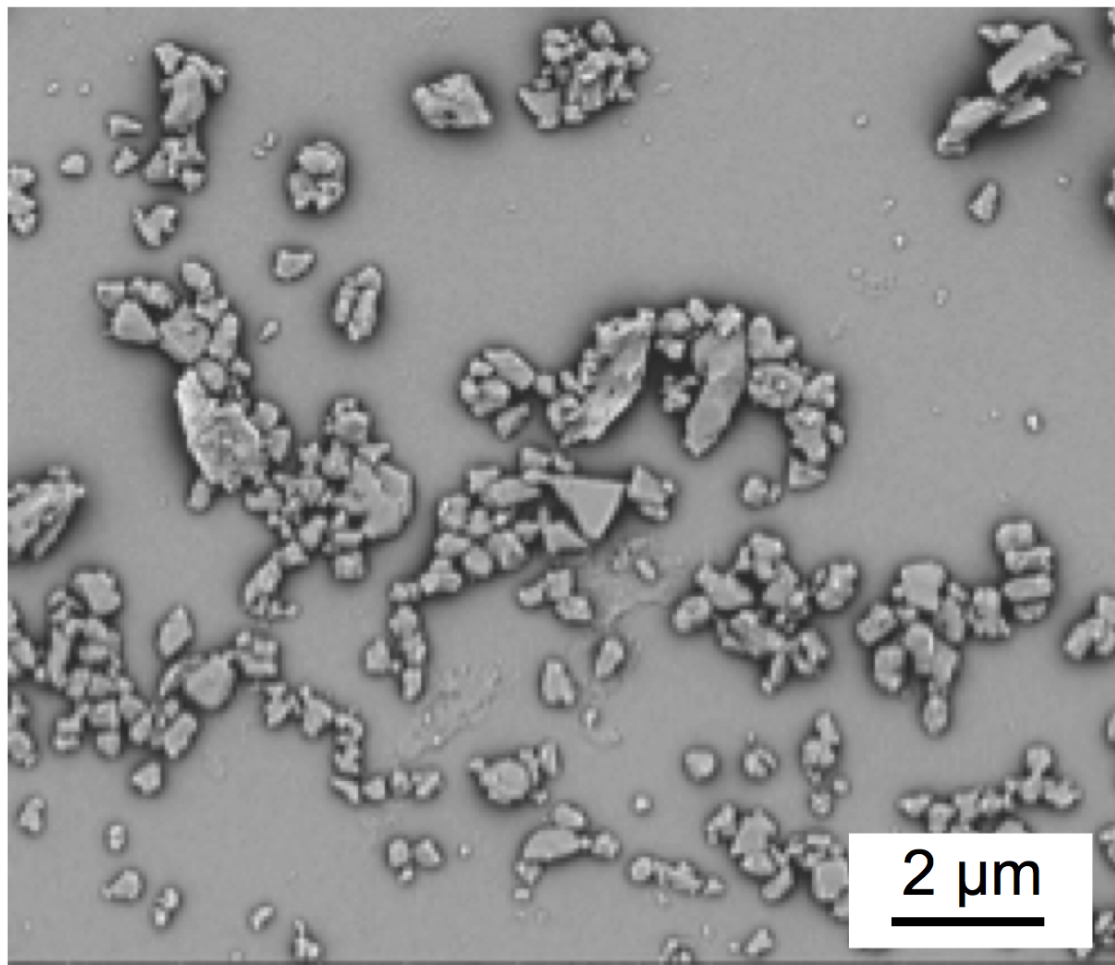


Figure 3.1. SEM image of 380 ppm MgO-doped specialty alumina powder used in this work.

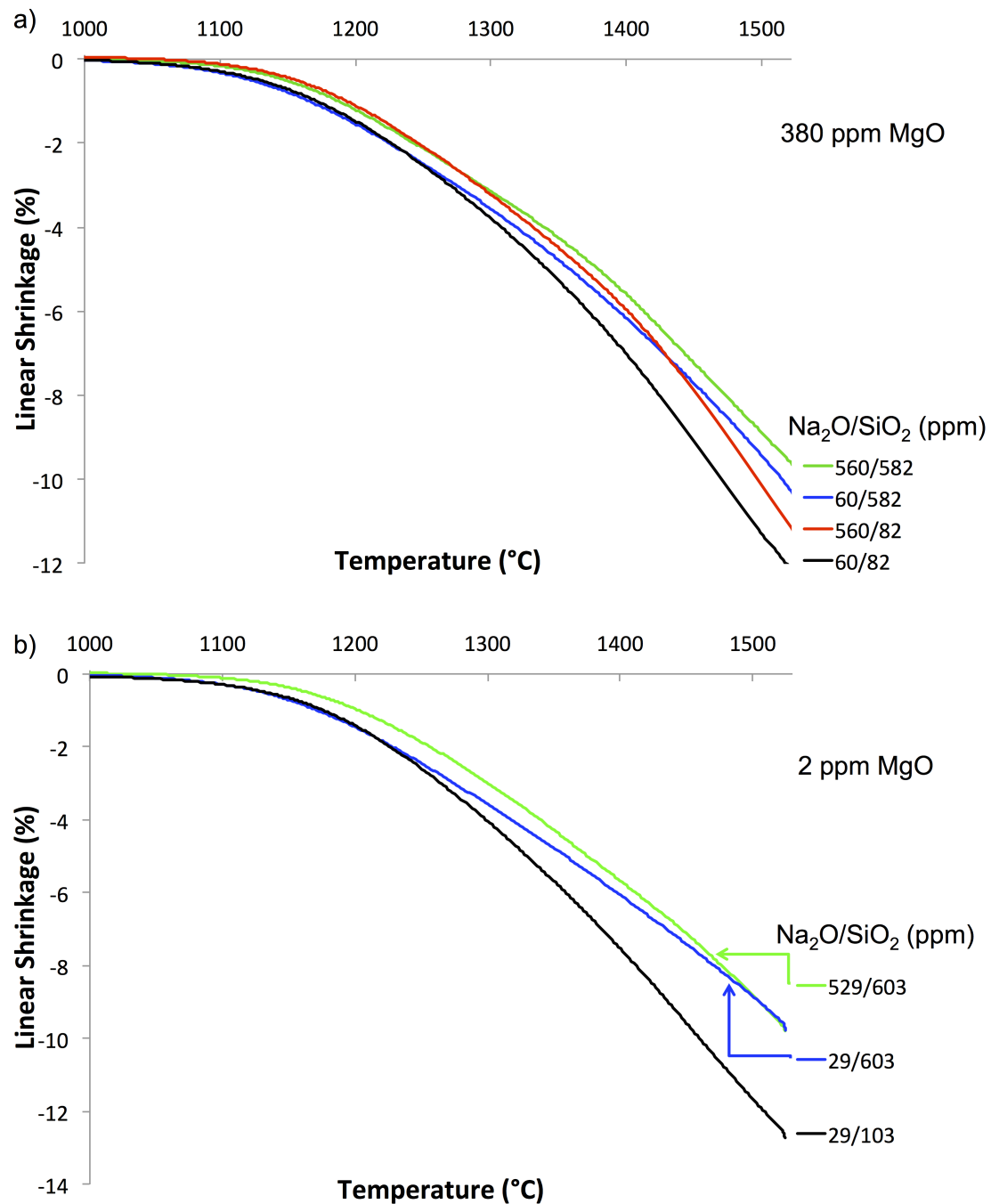


Figure 3.2. Dilatometer curves of a) 380 ppm MgO-doped and b) MgO-free [1] specialty alumina samples with different $\text{Na}_2\text{O}/\text{SiO}_2$ levels heated at 10°C/min to 1525°C.

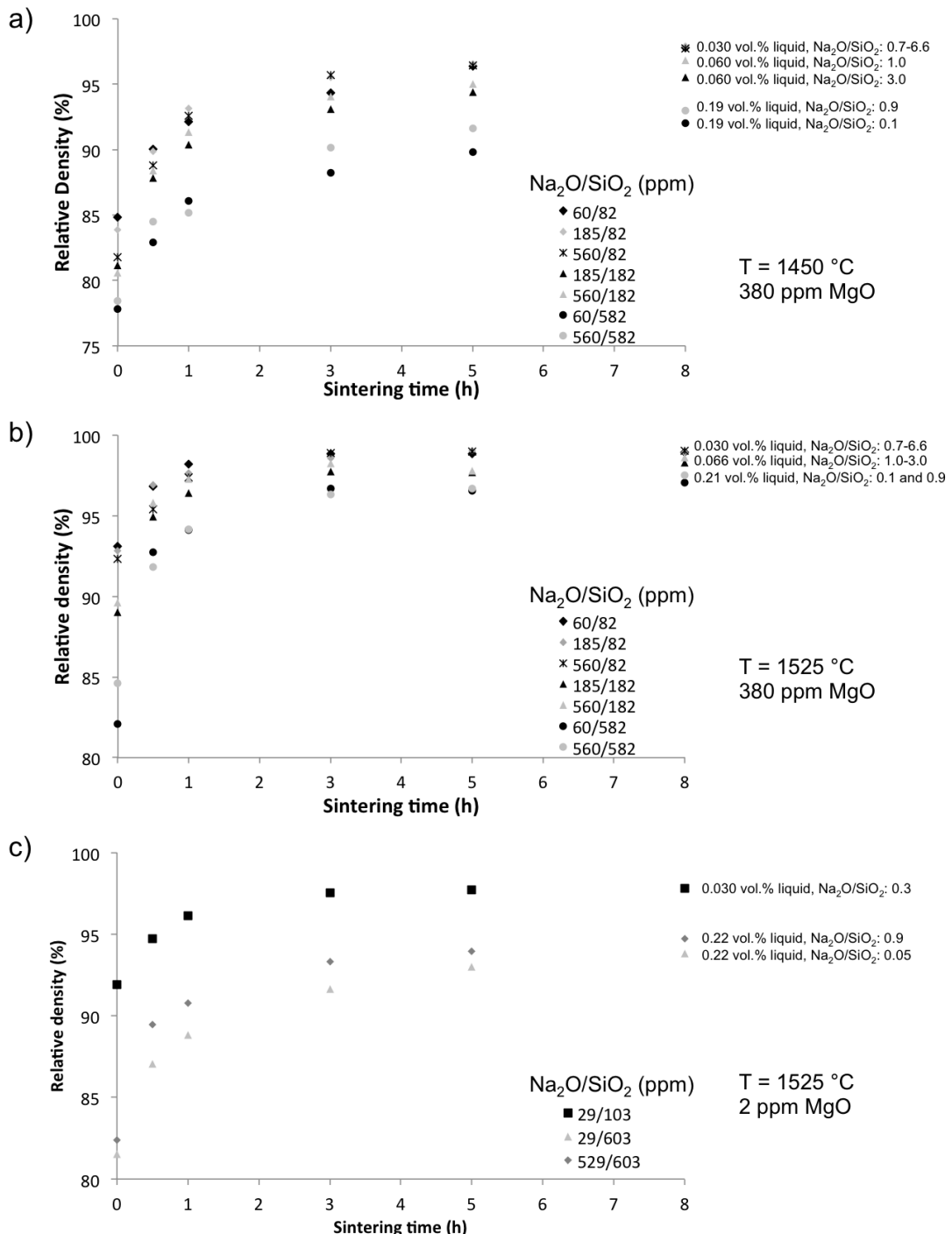


Figure 3.3. Densification kinetics of specialty processed alumina containing different amounts Na_2O and SiO_2 and a) 380 ppm MgO sintered at 1450°C , b) 380 ppm MgO sintered at 1525°C , and c) 2 ppm MgO sintered at 1525°C [1].

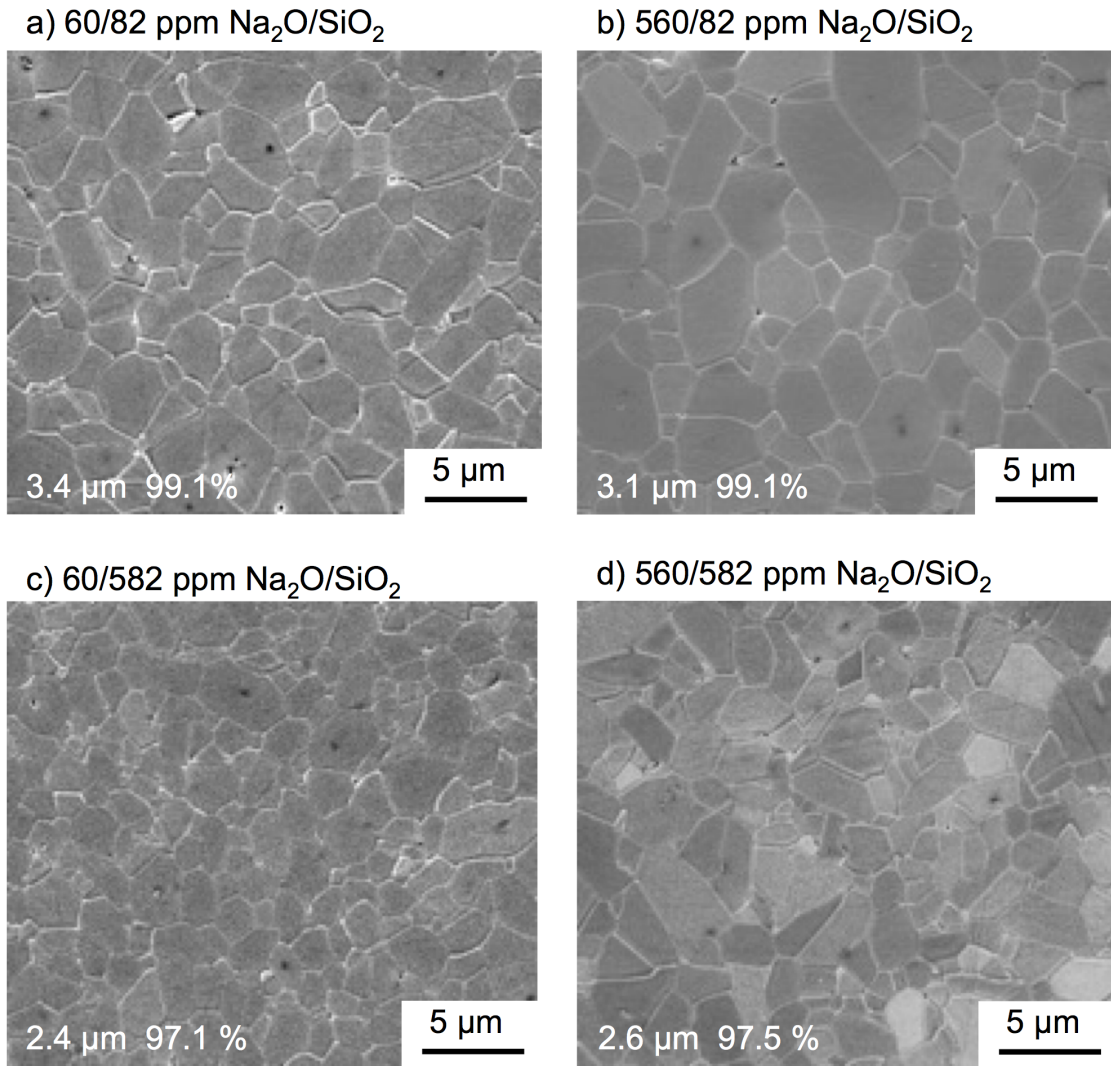


Figure 3.4. Microstructures of 380 ppm MgO-doped specialty alumina samples with different Na_2O and SiO_2 concentrations sintered at 1525°C for 8 h.

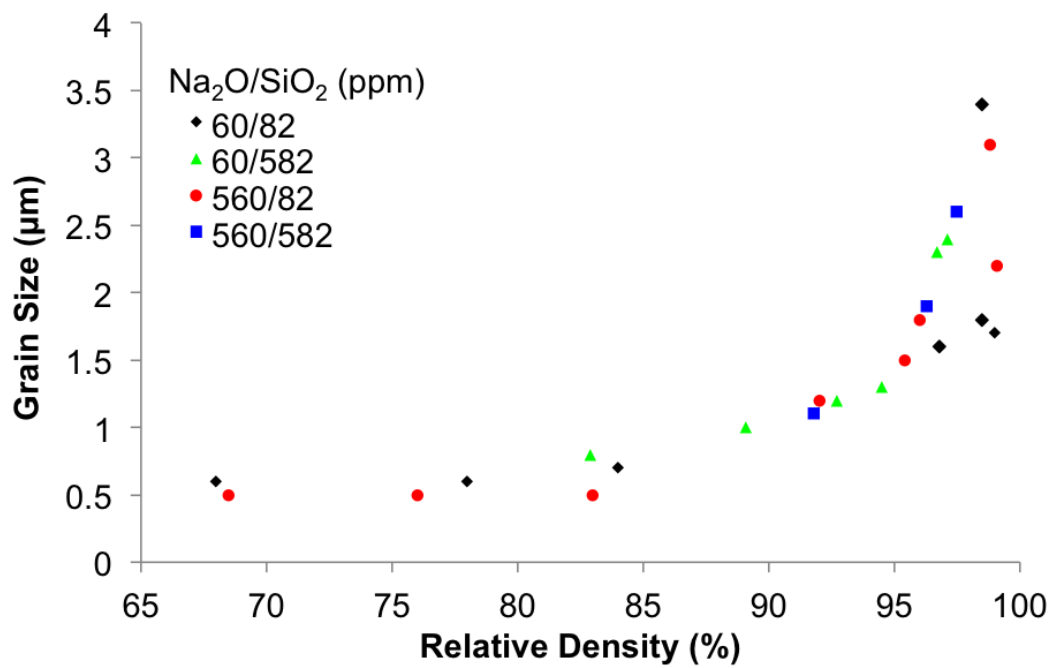


Figure 3.5. Sintering trajectories (grain size vs. relative density) for 380 ppm MgO-doped specialty alumina samples with different Na₂O and SiO₂ concentrations.

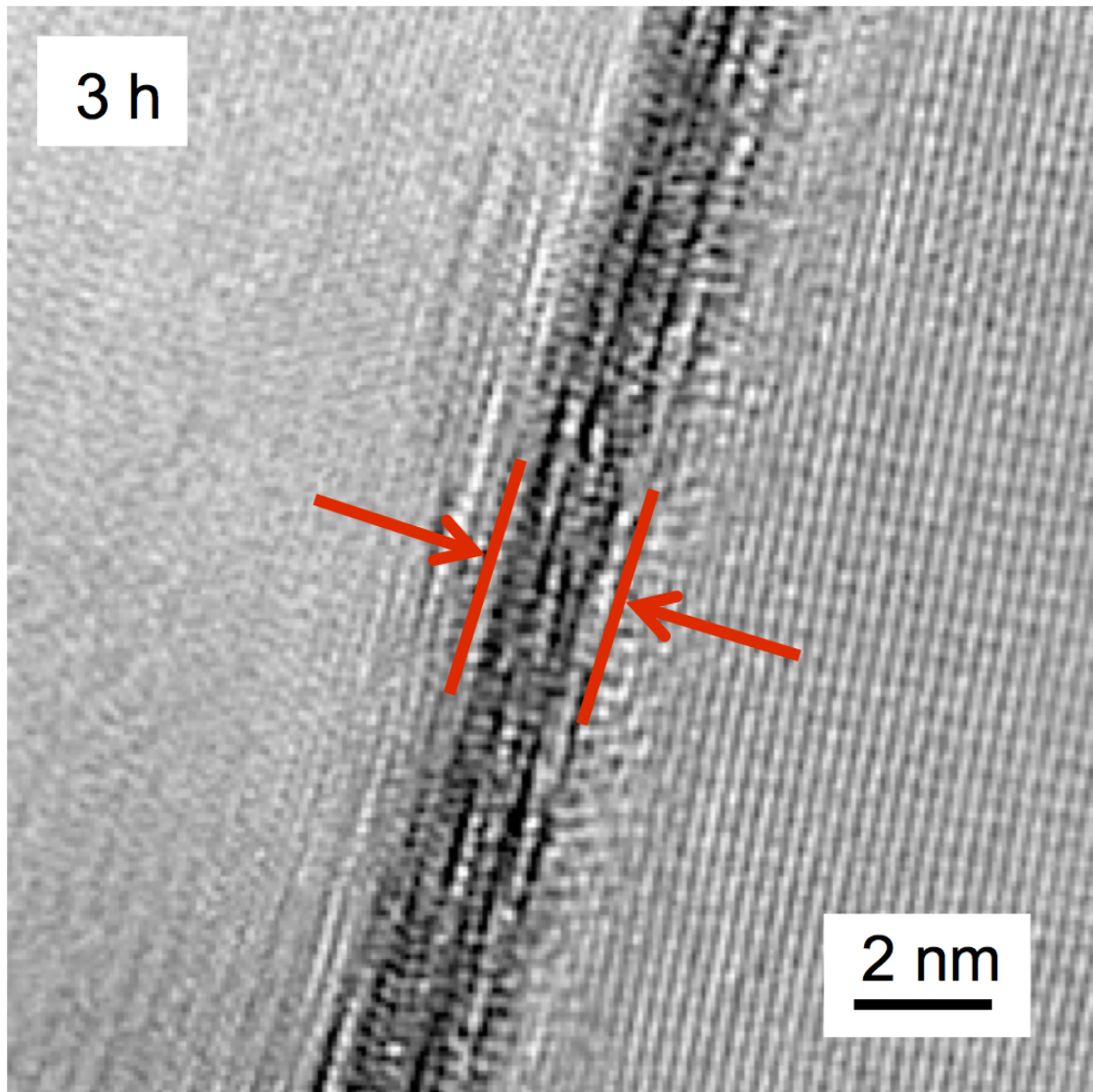


Figure 3.6. Grain boundary of a sample containing 529 ppm Na₂O, 603 ppm SiO₂, and 2 ppm MgO after 3 h at 1525°C.

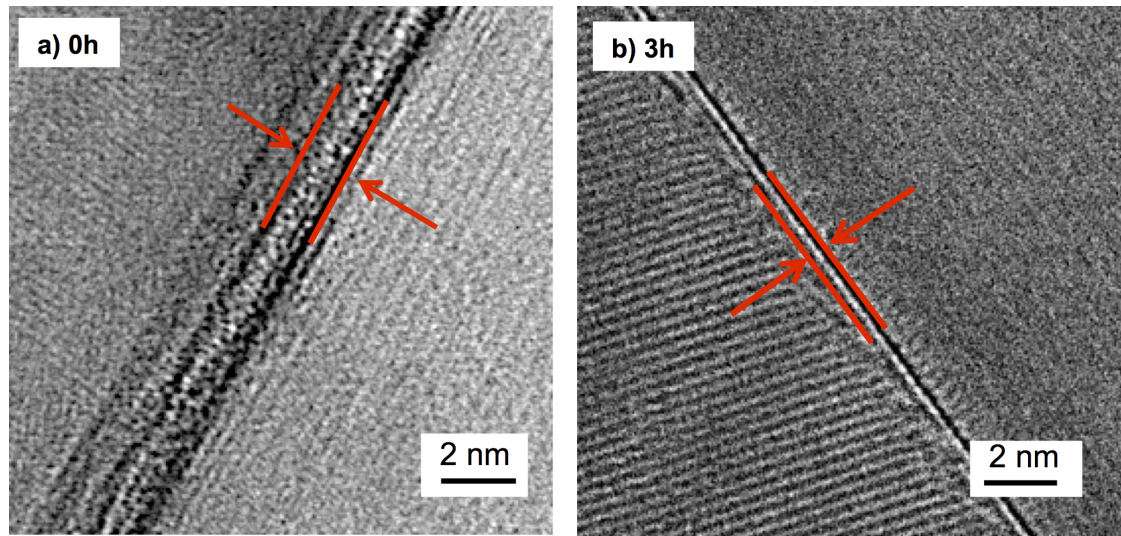


Figure 3.7. Grain boundaries of samples containing 560 ppm Na₂O, 582 ppm SiO₂, and 380 ppm MgO after a) 0 h and b) 3 h at 1525°C.

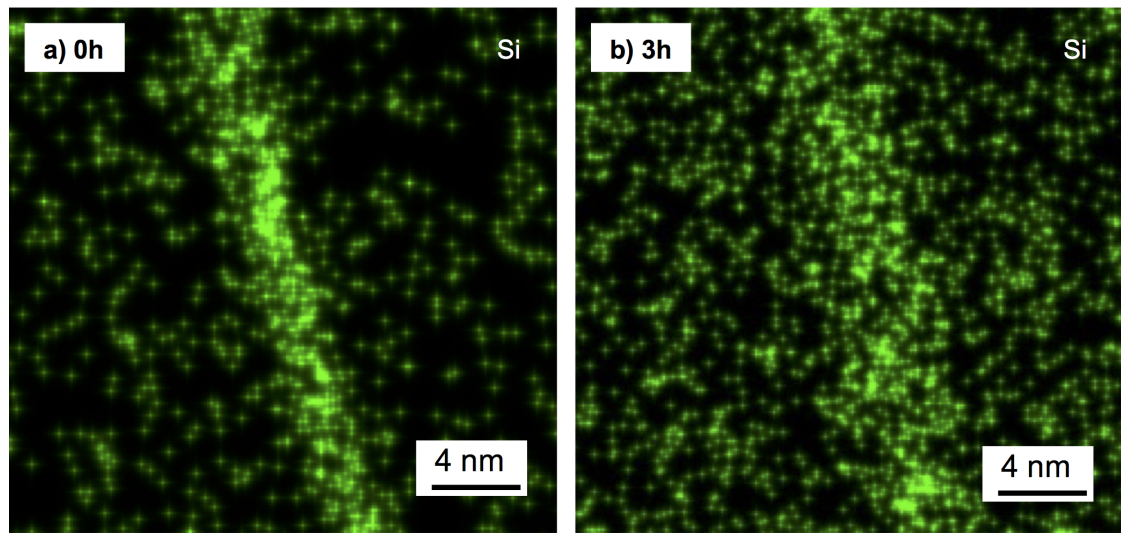


Figure 3.8. EDS of grain boundaries of samples containing 560 ppm Na₂O, 582 ppm SiO₂, and 380 ppm MgO after a) 0 h and b) 3 h at 1525°C showing the Si distribution. After 0 h Si shows a stronger segregation to the grain boundaries than after 3 h.

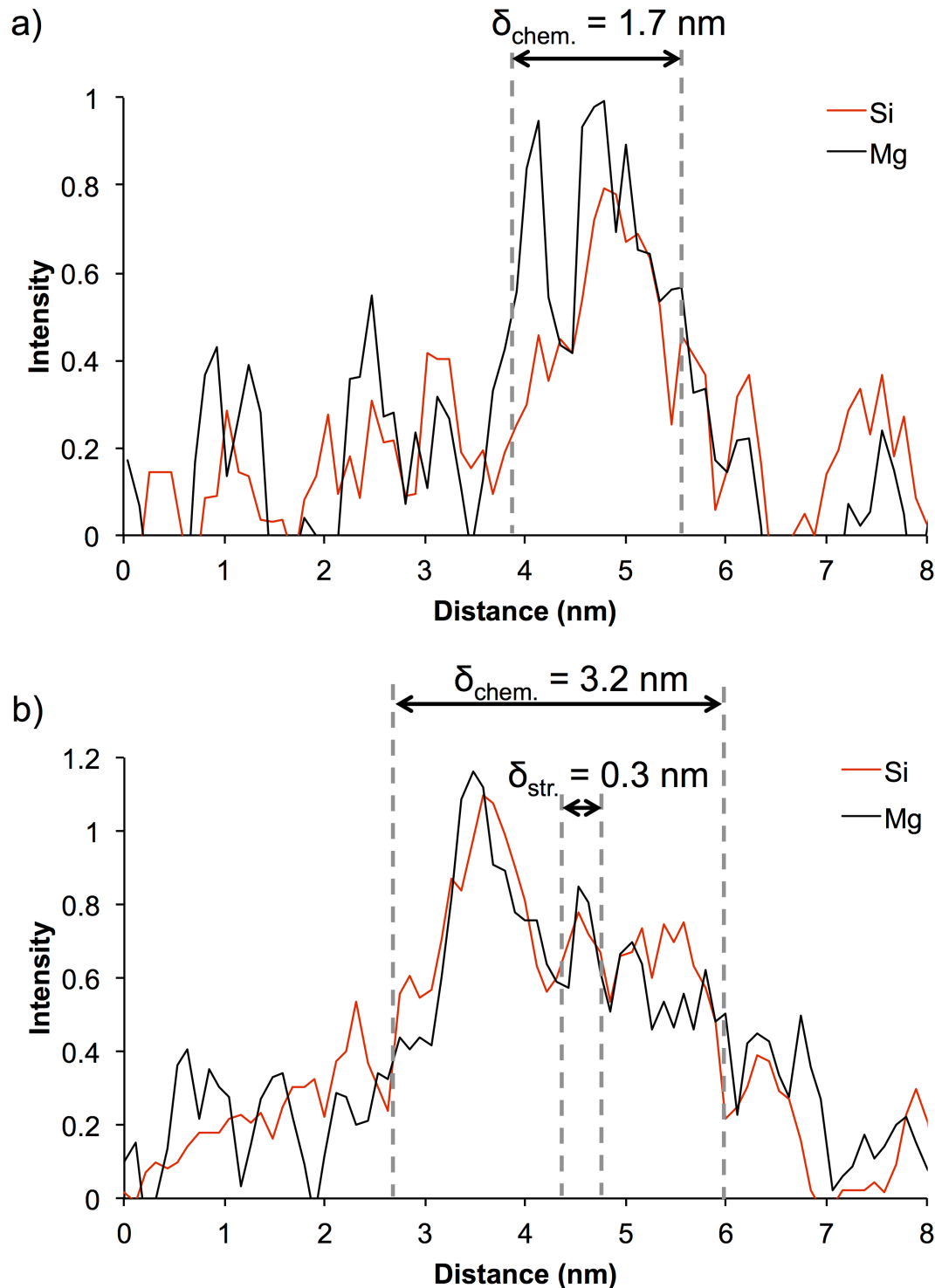


Figure 3.9. EDS line scan across a grain boundary of a sample containing 560 ppm Na₂O, 582 ppm SiO₂, and 380 ppm MgO after sintering at 1525°C for a) 0 h and b) 3 h.

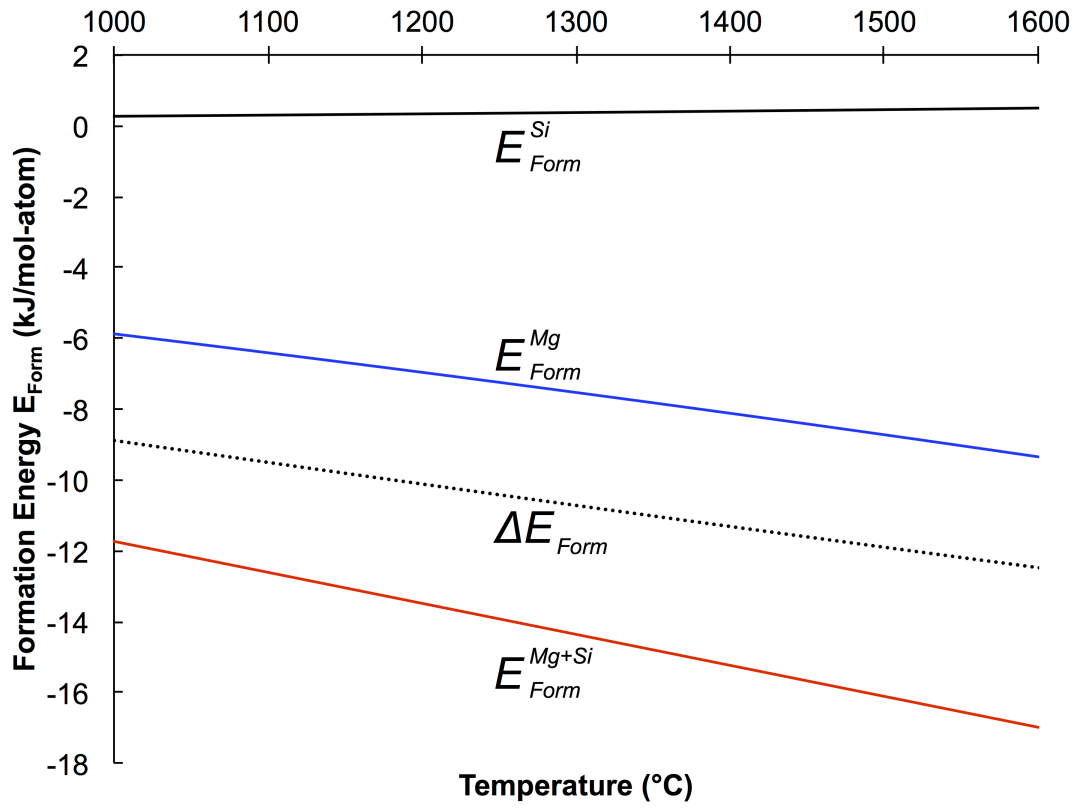


Figure 3.10. Comparison of the formation energy of alpha-Al₂O₃ with an Mg-cluster (E_{Form}^{Mg}), Si-cluster (E_{Form}^{Si}) and Mg+Si-cluster (E_{Form}^{Mg+Si}) as a function of temperature. The formation energy difference (ΔE_{Form}) between the structures was calculated from Eq. REF to compare the formation energy values and show that it is energetically favorable to form Mg+Si-clusters over Si-clusters and Mg-clusters.

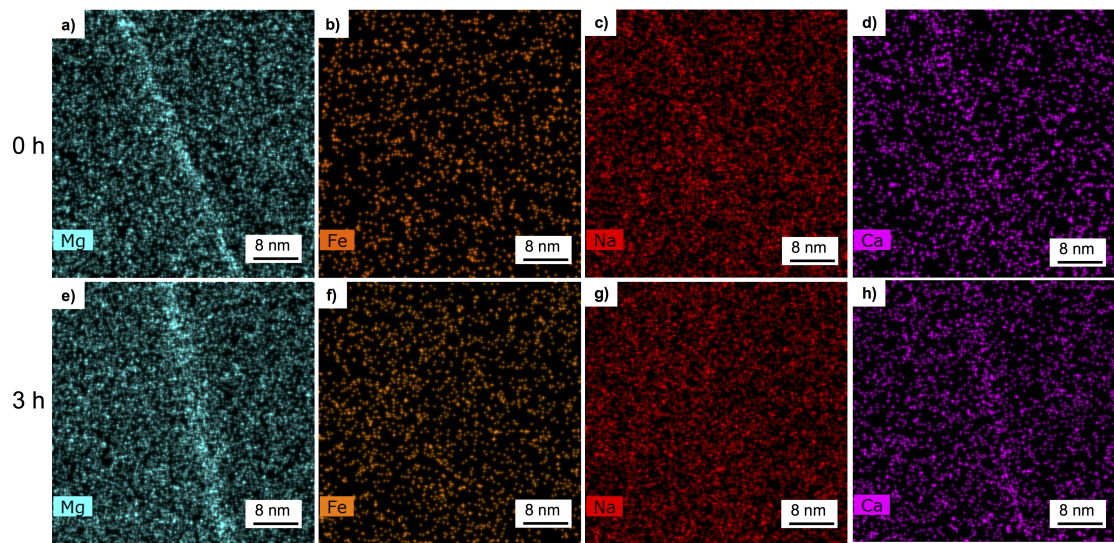


Figure 3.11. EDS maps of different oxides in 380 ppm MgO-doped specialty alumina samples after sintering at 1525°C for a-d) 0 h and e-h) 3 h.

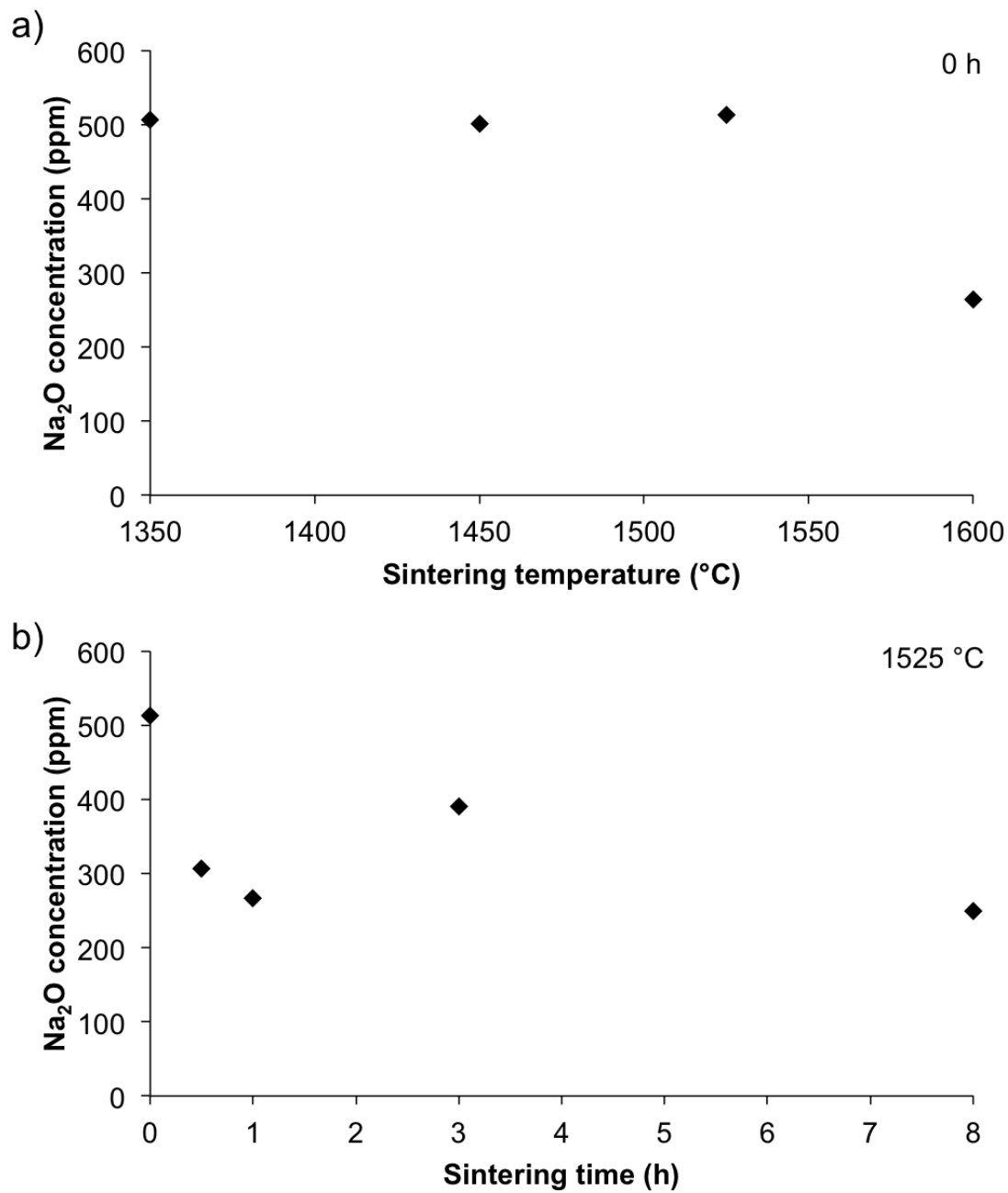


Figure 3.12. Na₂O concentration (ICP measurements) of 380 ppm MgO-doped specialty alumina samples with 560 ppm Na₂O as a) function of sintering temperature and b) as a function of sintering time at 1525 °C.

Chapter 4 | Powder Chemistry Effects on Grain Boundaries During Den- sification of Bayer Alumina

4.1 Introduction

When in the Course of human events, it becomes necessary for one people to dissolve the political bands which have connected them with another, and to assume among the powers of the earth, the separate and equal station to which the Laws of Nature and of Nature's God entitle them, a decent respect to the opinions of mankind requires that they should declare the causes which impel them to the separation.

4.2 More Declaration

We hold these truths to be self-evident, that all men are created equal, that they are endowed by their Creator with certain unalienable Rights, that among these are Life, Liberty and the pursuit of Happiness. –That to secure these rights, Governments are instituted among Men, deriving their just powers from the consent of the governed, –That whenever any Form of Government becomes destructive of these ends, it is the Right of the People to alter or to abolish it, and to institute new Government, laying its foundation on such principles and organizing its powers in such form, as to them shall seem most likely to effect their Safety and Happiness. Prudence, indeed, will dictate that Governments long established should not be

changed for light and transient causes; and accordingly all experience hath shewn, that mankind are more disposed to suffer, while evils are sufferable, than to right themselves by abolishing the forms to which they are accustomed. But when a long train of abuses and usurpations, pursuing invariably the same Object evinces a design to reduce them under absolute Despotism, it is their right, it is their duty, to throw off such Government, and to provide new Guards for their future security. —Such has been the patient sufferance of these Colonies; and such is now the necessity which constrains them to alter their former Systems of Government. The history of the present King of Great Britain [George III] is a history of repeated injuries and usurpations, all having in direct object the establishment of an absolute Tyranny over these States. To prove this, let Facts be submitted to a candid world.

Chapter 5 |

β -Al₂O₃: A Model System for the Formation of Second Phases in Al₂O₃

5.1 Introduction

When in the Course of human events, it becomes necessary for one people to dissolve the political bands which have connected them with another, and to assume among the powers of the earth, the separate and equal station to which the Laws of Nature and of Nature's God entitle them, a decent respect to the opinions of mankind requires that they should declare the causes which impel them to the separation.

5.2 More Declaration

We hold these truths to be self-evident, that all men are created equal, that they are endowed by their Creator with certain unalienable Rights, that among these are Life, Liberty and the pursuit of Happiness. –That to secure these rights, Governments are instituted among Men, deriving their just powers from the consent of the governed, –That whenever any Form of Government becomes destructive of these ends, it is the Right of the People to alter or to abolish it, and to institute new Government, laying its foundation on such principles and organizing its powers in such form, as to them shall seem most likely to effect their Safety and Happiness. Prudence, indeed, will dictate that Governments long established should not be

changed for light and transient causes; and accordingly all experience hath shewn, that mankind are more disposed to suffer, while evils are sufferable, than to right themselves by abolishing the forms to which they are accustomed. But when a long train of abuses and usurpations, pursuing invariably the same Object evinces a design to reduce them under absolute Despotism, it is their right, it is their duty, to throw off such Government, and to provide new Guards for their future security. —Such has been the patient sufferance of these Colonies; and such is now the necessity which constrains them to alter their former Systems of Government. The history of the present King of Great Britain [George III] is a history of repeated injuries and usurpations, all having in direct object the establishment of an absolute Tyranny over these States. To prove this, let Facts be submitted to a candid world.

Chapter 6 |

Challenges and Opportunities of Master Sintering Curve Anal- ysis of Sintering Processes

6.1 Introduction

When in the Course of human events, it becomes necessary for one people to dissolve the political bands which have connected them with another, and to assume among the powers of the earth, the separate and equal station to which the Laws of Nature and of Nature's God entitle them, a decent respect to the opinions of mankind requires that they should declare the causes which impel them to the separation.

6.2 Experimental

Chapter 7 |

Summary and Future Work

7.1 Introduction

When in the Course of human events, it becomes necessary for one people to dissolve the political bands which have connected them with another, and to assume among the powers of the earth, the separate and equal station to which the Laws of Nature and of Nature's God entitle them, a decent respect to the opinions of mankind requires that they should declare the causes which impel them to the separation.

7.2 More Declaration

We hold these truths to be self-evident, that all men are created equal, that they are endowed by their Creator with certain unalienable Rights, that among these are Life, Liberty and the pursuit of Happiness. —That to secure these rights, Governments are instituted among Men, deriving their just powers from the consent of the governed, —That whenever any Form of Government becomes destructive of these ends, it is the Right of the People to alter or to abolish it, and to institute new Government, laying its foundation on such principles and organizing its powers in such form, as to them shall seem most likely to effect their Safety and Happiness. Prudence, indeed, will dictate that Governments long established should not be changed for light and transient causes; and accordingly all experience hath shewn, that mankind are more disposed to suffer, while evils are sufferable, than to right themselves by abolishing the forms to which they are accustomed. But when a long train of abuses and usurpations, pursuing invariably the same Object evinces

a design to reduce them under absolute Despotism, it is their right, it is their duty, to throw off such Government, and to provide new Guards for their future security. —Such has been the patient sufferance of these Colonies; and such is now the necessity which constrains them to alter their former Systems of Government. The history of the present King of Great Britain [George III] is a history of repeated injuries and usurpations, all having in direct object the establishment of an absolute Tyranny over these States. To prove this, let Facts be submitted to a candid world.

Bibliography

- [1] BAE, I.-J. and S. BAIK (1997) “Abnormal grain growth of alumina,” **56**(192101), pp. 1149–1156.
- [2] LOUET, N., M. GONON, and G. FANTOZZI (2005) “Influence of the amount of Na₂O and SiO₂ on the sintering behavior and on the microstructural evolution of a Bayer alumina powder,” *Ceramics international*, **31**(7), pp. 981–987.
- [3] STANDARD, A. (2015) “B962-15 Standard Test Method for Density of Compacted or Sintered Powder Metallurgy (PM) Products Using Archimedes’ Principle,” .
URL www.astm.org
- [4] ——— (2013) “E112-13: Standard Test Methods for Determining Average Grain Size,” *West Conshocken*.
URL www.astm.org
- [5] JUDD, M., B. PLUNKETT, and M. POPE (1974) “The thermal decomposition of calcium, sodium, silver and copper (II) acetates,” *Journal of Thermal Analysis and Calorimetry*, **6**(5), pp. 555–563.
- [6] LAMBOTTE, G. and P. CHARTRAND (2013) “Thermodynamic modeling of the (Al₂O₃+Na₂O),(Al₂O₃+Na₂O+SiO₂), and (Al₂O₃+Na₂O+AlF₃+NaF) systems,” *The Journal of Chemical Thermodynamics*, **57**, pp. 306–334.
- [7] BROWNMILLER, L. T. and R. H. BOGUE (1932) “The system CaO-Na₂O-Al₂O₃,” *American Journal of Science*, (138), pp. 501–524.
- [8] PABLOÁRGALAN, L. and W. R. FOSTER (1959) “Investigation of Role of Beta Alumina in the System Na₂O-Al₂O₃-SiO₂,” *Journal of the American Ceramic Society*, **42**(10), pp. 491–498.
- [9] RANKIN, G. A. and H. E. MERWIN (1916) “THE TERNARY SYSTEM CaO-Al₂O₃-MgO.” *Journal of the American Chemical Society*, **38**(3), pp. 568–588.

- [10] RIDGWAY, R. R., A. A. KLEIN, and W. J. O'LEARY (1936) "The Preparation and Properties of SoâĂŖCalled âĂĲBeta AluminaâĂĪ," *Transactions of the Electrochemical Society*, **70**(1), pp. 71–88.
- [11] DUNCAN, J. H. and W. E. C. CREYKE (1969) "FORMATION AND STABILITY OF BETA-AL₂O₃ IN ALPHA-AL₂O₃ CERAMICS," *TRANSACTIONS OF THE BRITISH CERAMIC SOCIETY*, **68**(3), p. 137.
- [12] SUTORIK, A. C., S. S. NEO, D. R. TREADWELL, and R. M. LAINE (1998) "Synthesis of Ultrafine β âĂşAlumina Powders via Flame Spray Pyrolysis of Polymeric Precursors," *Journal of the American Ceramic Society*, **81**(6), pp. 1477–1486.
- [13] STEVENS, R. and J. G. P. BINNER (1984) "Structure, properties and production of β -alumina," *Journal of materials science*, **19**(3), pp. 695–715.
- [14] CHRISTIE, J. R., A. J. DARNELL, and D. F. DUSTIN (1978) "Reaction of molten sodium carbonate with aluminum oxide," *J. Phys. Chem.;(United States)*, **82**(1).
- [15] KUMMER, J. T. (1972) " β -alumina electrolytes," *Progress in solid state chemistry*, **7**, pp. 141–175.
- [16] VRIES, R. C. and W. L. ROTH (1969) "Critical Evaluation of the Literature Data on Beta Alumina and Related Phases: I, Phase Equilibria and Characterization of Beta Alumina Phases," *Journal of the American Ceramic Society*, **52**(7), pp. 364–369.
- [17] TERAI, R. and R. HAYAMI (1975) "Ionic diffusion in glasses," *Journal of Non-Crystalline Solids*, **18**(2), pp. 217–264.
- [18] KWON, O. and G. L. MESSING (1990) "Kinetic Analysis of SolutionâĂŖPrecipitation During LiquidâĂŖPhase Sintering of Alumina," *Journal of the American Ceramic Society*, **73**(2), pp. 275–281.
- [19] KWON, O.-H. and G. L. MESSING (1991) "A theoretical analysis of solution-precipitation controlled densification during liquid phase sintering," *Acta metallurgica et materialia*, **39**(9), pp. 2059–2068.
- [20] PARK, C. W. and D. Y. YOON (2000) "Effects of SiO₂, CaO₂, and MgO additions on the grain growth of alumina," *Journal of the American ceramic society*, **83**(10), pp. 2605–2609.
- [21] DAY, D. E. and G. E. RINDONE (1962) "Properties of soda aluminosilicate glasses: I, refractive index, density, molar refractivity, and infrared absorption spectra," *Journal of the American Ceramic Society*, **45**(10), pp. 489–496.

- [22] WU, G., E. YAZHENSKIHKH, K. HACK, and M. MÜLLER (2015) “Viscosity model for oxide melts relevant to fuel slags. Part 2: The system SiO₂-Al₂O₃-CaO-MgO-Na₂O-K₂O,” *Fuel Processing Technology*, **138**, pp. 520–533.
- [23] POPOVIC, A., L. BENCZE, J. KORUZA, B. MALIC, and M. KOSEC (2012) “Knudsen effusion mass spectrometric approach to the thermodynamics of Na₂O-Nb₂O₅ system,” *International Journal of Mass Spectrometry*, **309**, pp. 70–78.
- [24] GALLUP, J. (1935) “The transformation of aluminum oxide from the beta to the alpha form,” *Journal of the American Ceramic Society*, **18**(1–12), pp. 144–148.
- [25] BAE, S. I. and S. BAIK (1994) “Critical concentration of MgO for the prevention of abnormal grain growth in alumina,” *Journal of the American Ceramic Society*, **77**(10), pp. 2499–2504.
- [26] ——— (1993) “Sintering and grain growth of ultrapure alumina,” *Journal of Materials Science*, **28**(15), pp. 4197–4204.
- [27] BENNISON, S. J. and M. P. HARMER (1990) “A history of the role of MgO in the sintering of alpha-Al₂O₃,” in *Ceramic Transactions 7, Sintering of Advanced Ceramics* (C. A. Handwerker, J. E. Blendell, and W. A. Kaysser, eds.), Am. Ceram. Soc., Westerville, pp. 13–49.
- [28] JORGENSEN, P. J. (1965) “Modification of sintering kinetics by solute segregation in Al₂O₃,” *Journal of the American Ceramic Society*, **48**(4), pp. 207–210.
- [29] HEUER, A. H. (1979) “The role of MgO in the sintering of alumina,” *Journal of the American Ceramic Society*, **62**, pp. 317–318.
- [30] PARK, C. W. and D. Y. YOON (2000) “Grain growth of alumina,” *609*(3), pp. 2605–2609.
- [31] FRUEH, T., E. KUPP, C. COMPSON, J. ATRIA, and G. MESSING (2016) “The effects of Na₂O and SiO₂ in liquid phase sintering of Bayer Al₂O₃,” *Journal of the American Ceramic Society*, **99**(7), pp. 2267–2272.
- [32] HANDWERKER, C. A., P. A. MORRIS, and R. L. COBLE (1989) “Effects of chemical inhomogeneities on grain growth and microstructure in Al₂O₃,” *Journal of the American Ceramic Society*, **72**(1), pp. 130–136.

- [33] GAVRILOV, K. L., S. J. BENNISON, K. R. MIKESKA, J. M. CHABALA, and R. LEVI-SETTI (1999) “Silica and magnesia dopant distributions in alumina by high-resolution scanning secondary ion mass spectrometry,” *Journal of the American Ceramic Society*, **82**(4), pp. 1001–1008.
- [34] SHANG, S., Y. WANG, D. KIM, and Z.-K. LIU (2010) “First-principles thermodynamics from phonon and Debye model: Application to Ni and Ni₃Al,” *Computational Materials Science*, **47**(4), pp. 1040–1048.
- [35] WANG, Y., Z.-K. LIU, and L.-Q. CHEN (2004) “Thermodynamic properties of Al, Ni, NiAl, and Ni₃Al from first-principles calculations,” *Acta Materialia*, **52**(9), pp. 2665–2671.
- [36] LIU, X. L., B. K. VANLEEUWEN, S. SHANG, Y. DU, and Z.-K. LIU (2015) “On the scaling factor in Debye–Grüneisen model: A case study of the Mg–Zn binary system,” *Computational Materials Science*, **98**, pp. 34–41.
- [37] SHANG, S., Y. WANG, and Z.-K. LIU (2007) “First-principles elastic constants of alpha- and theta-Al₂O₃,” *Applied Physics Letters*, **90**(10), pp. 101909–1–101909–3.
- [38] KRESSE, G. and J. FURTHMÜLLER (1996) “Efficiency of ab-initio total energy calculations for metals and semiconductors using a plane-wave basis set,” *Computational Materials Science*, **6**(1), pp. 15–50.
- [39] KRESSE, G. and D. JOUBERT (1999) “From ultrasoft pseudopotentials to the projector augmented-wave method,” *Physical Review B*, **59**(3), pp. 1758–1775.
- [40] BLÖCHL, P. (1994) “Projector augmented-wave method,” *Physical Review B*, **50**(24), p. 17953.
- [41] PERDEW, J. and Y. WANG (1992) “Accurate and simple analytic representation of the electron-gas correlation energy,” *Physical Review B*, **45**(23), p. 13244.
- [42] MONKHORST, H. and J. PACK (1976) “Special points for Brillouin-zone integrations,” *Physical Review B*, **13**(12), pp. 5188–5192.
- [43] ATKINSON, K. J. W., R. W. GRIMES, M. R. LEVY, Z. L. COULL, and T. ENGLISH (2003) “Accommodation of impurities in α -Al₂O₃, α -Cr₂O₃ and α -Fe₂O₃,” *Journal of the European Ceramic Society*, **23**(16), pp. 3059–3070.
- [44] GRIMES, R. W. (1994) “Solution of MgO, CaO, and TiO₂ in α -Al₂O₃,” *Journal of the American Ceramic Society*, **77**(2), pp. 378–384.
- [45] LAGERLÖF, K. P. D. and R. W. GRIMES (1998) “The defect chemistry of sapphire (α -Al₂O₃),” *Acta materialia*, **46**(16), pp. 5689–5700.

- [46] XIANG, X., G. ZHANG, X. WANG, T. TANG, and Y. SHI (2015) “A new perspective on the process of intrinsic point defects in α -Al₂O₃,” *Physical Chemistry Chemical Physics*, **17**(43), pp. 29134–29141.
- [47] SARSAM, J., M. W. FINNIS, and P. TANGNEY (2013) “Atomistic force field for alumina fit to density functional theory,” *The Journal of chemical physics*, **139**(20), p. 204704.
- [48] MAO, H., O. FABRICHNAYA, M. SELLEBY, and B. SUNDMAN (2005) “Thermodynamic assessment of the MgO-Al₂O₃-SiO₂ system,” *Journal of Materials Research*, **20**(04), pp. 975–986.
- [49] SUBRAMANIAM, A., C. T. KOCH, R. M. CANNON, and M. RÜHLE (2006) “Intergranular glassy films: An overview,” *Materials Science and Engineering A*, **422**(1-2), pp. 3–18.
- [50] JAIN, A., S. ONG, G. HAUTIER, W. CHEN, W. RICHARDS, S. DACEK, S. CHOLIA, D. GUNTER, D. SKINNER, and G. CEDER (2013) “The Materials Project: A materials genome approach to accelerating materials innovation,” *Apl Materials*, **1**(1), p. 11002.
- [51] “Materials Project,” .
URL <http://www.materialsproject.org>
- [52] GRAHAM, J. (1960) “Lattice spacings and colour in the system alumina - chromic oxide,” *Journal of Physics and Chemistry of Solids*, **12**, pp. 349–350.
- [53] BERGERHOFF, G., R. HUNDT, R. SIEVERS, and I. D. BROWN (1983) “The inorganic crystal structure data base,” *Journal of Chemical Information and Computer Sciences*, **23**(2), pp. 66–69.
- [54] KARLSRUHE, F. I. Z., “Inorganic Crystal Structure Database,” .
- [55] RAGHAVAN, V. (2010) “Al-Fe-O (Aluminum-iron-oxygen),” *Journal of Phase Equilibria and Diffusion*, **31**(4), p. 367.

Vita

Tobias Frueh

The details of my childhood are inconsequential.